An efficient high-order bound-preserving explicit-implicit-null time integration for the Richards equation in unsaturated geotechnical media

Xinyu Wu[a], Juan Cheng[b,1,*], Hui Guo[c,2], Chi-Wang Shu[d,3]

[a] *Graduate School, China Academy of Engineering Physics, Beijing, 100088, China*
[b] *Academy for Multidisciplinary Studies, Capital Normal University, Beijing, 100048, China*
[c] *College of Science, China University of Petroleum, Qingdao, 266580, China*
[d] *Division of Applied Mathematics, Brown University, Providence, RI 02912, USA*

Abstract

To address the computational bottlenecks in efficient, accurate, and robust simulations of the Richards equation for unsaturated flow in geotechnical media, we propose a third-order explicit-implicit-null (EIN) time integration method. For spatial discretization, a conservative high-order finite-difference multi-resolution weighted essentially non-oscillatory (WENO) scheme is constructed to accurately resolve sharp wetting fronts and suppress spurious oscillations. The core idea of the EIN framework is to add and subtract a suitably large Laplacian operator at one side of the Richards equation, followed by an implicit-explicit (IMEX) time-marching strategy that treats the added linear diffusion term implicitly and all other terms explicitly. This treatment significantly relaxes the time-step restriction and completely avoids costly nonlinear iterations, substantially improving computational efficiency, especially for large-scale and three-dimensional (3D) problems. To further ensure physical rationality and numerical robustness, a bound-preserving sweeping technique is incorporated to maintain solutions within physical bounds, while preserving conservation and accuracy. The proposed algorithm is easy to implement and readily integrable into geotechnical applications. The performance and practical applicability are demonstrated by a series of numerical experiments, ranging from canonical infiltration benchmarks to challenging 3D application problems in layered and heterogeneous soils, including a realistic case using field-sampled black soil parameters from Northeast China.

Keywords: Richards equation, Explicit-implicit-null time discretization, Multi-resolution WENO scheme, Bound-preserving, High order accuracy, Unsaturated flow

*Corresponding author

Email addresses: wuxinyu24@gscaep.ac.cn (Xinyu Wu), jcheng@cnu.edu.cn (Juan Cheng), sdugh@163.com (Hui Guo), chi-wang_shu@brown.edu (Chi-Wang Shu)

[1]Research is supported in part by National Key R&D Program of China No. 2023YFA1009003, and NSFC grant 12571432.

[2]Research is supported in part by National Key R&D Program of China No. 2023YFA1009003.

[3]Research is supported in part by NSF grant DMS-2309249.

1. Introduction

Reliable numerical simulation of unsaturated flow in geotechnical media is critical for numerous scientific applications, such as slope stability, landfill design, embankment performance, and subsurface contamination. Such flow processes, driven by gravitational and capillary effects, are typically governed by the Richards equation [46], a highly nonlinear and time-dependent partial differential equation (PDE). Numerical methods provide a powerful tool for its solution, yet considerable challenges persist in achieving satisfactory accuracy, robustness, and computational efficiency, especially for large-scale and 3D application problems.

A variety of numerical methods have been developed for the Richards equation, including finite element method (FEM) [1, 10, 42, 50], finite volume method (FVM) [22, 40, 51, 52] and finite difference method (FDM) [11, 14, 20, 47]. These approaches often face challenges in simultaneously achieving high-order accuracy, mass conservation, and oscillation-free resolution of sharp wetting fronts. Notably, hyperbolic behavior may emerge when the convection term becomes dominant or the diffusion term undergoes degeneration [24]. Some other techniques have also been implemented, such as the Eulerian-Lagrangian approach [24], mixed finite element methods [2, 6, 31], the local discontinuous Galerkin (LDG) method [36], and meshless techniques [7, 8]. However, the accuracy achieved in most of these works does not exceed second-order. To accurately capture the dynamics of wetting fronts, weighted essentially non-oscillatory (WENO) methods [4, 27, 37, 49] provide exceptional performance, delivering high-order accuracy in smooth regions while effectively suppressing non-physical oscillations near steep gradients and discontinuities. Recently, Zhu and Shu [68] proposed a new type of multi-resolution WENO (MRWENO) schemes, featuring unequal-sized stencils and linear weights that can be any positive numbers provided their sum equals 1. Such flexibility simplifies the procedure in applications of WENO schemes, enabling ready extension to arbitrary high-order accuracy and higher dimensions.

Beyond steep wetting fronts, solutions to the Richards equation also satisfy a bound-preserving (BP) property, i.e., the moisture content $\theta \in [\theta_r, \theta_s]$ and the unsaturated pressure head $\psi \leq 0$. Enforcing such physical bounds is essential for numerical stability and robustness. However, high-

order schemes do not inherently preserve such constraints. To address this issue, various BP methods have been developed, including scaling limiter [65–67], flux limiter [26, 59, 60], sweeping technique [38], and convex limiting [19, 33]. Capable of achieving BP properties without compromising conservation or high-order accuracy, these methods have been widely applied to physically constrained systems. However, to the best of our knowledge, few studies have focused on the BP techniques for Richards equation. In our recent work [58], a high-order BP finite-difference MR-WENO method was proposed for Richards equation that achieves fourth- and sixth-order spatial accuracy. A parameterized flux limiter was introduced to guarantee physical admissibility of the numerical solution. Nevertheless, the time discretization adopted in [58] is the explicit strong-stability-preserving (SSP) Runge–Kutta (RK) time discretization, which is easy to implement and easily complies with the parameterized flux limiter for bound preserving, but involves small time step restriction for stability, especially if diffusion is dominant in part of the computational domain. This motivates the development of a more efficient time-marching method, which is the core focus of this work.

Given the strong nonlinearity and stiffness of the Richards equation, a proper treatment of the temporal derivative is crucial for efficiently computing reliable numerical solutions. Explicit time schemes [21, 43, 58, 61] avoid nonlinear iterations, yet suffer from the stability constraint $\Delta t = O(h^2)$ imposed by the Courant–Friedrichs–Lewy (CFL) condition due to the diffusion term, where Δt is the time step and h is the mesh size. Such an extremely small time step leads to low computational efficiency for large-scale simulations or fine grid discretizations. Therefore, most current studies employ implicit schemes owing to the large time steps afforded by unconditional stability, such as the backward Euler method [2, 6, 29, 44], Crank-Nicolson scheme [12, 45], and implicit RK scheme [48]. Implicit schemes require solving nonlinear algebraic systems at each time step (typically via Newton or Picard iterations), not only incurring high costs but also posing significant implementation challenges for spatially high-order schemes. More critically, the iterative procedure may fail to converge due to the nonlinearity of soil constitutive laws [13, 30, 35]. The drawbacks of fully explicit and fully implicit methods underscore the importance

of exploring time integration methods that combine the strengths of both strategies. The explicit-implicit (IMEX) method [32] is a typical example, which treats the diffusion terms implicitly and convection terms explicitly, thus avoiding severe parabolic restrictions on the maximum admissible time step. However, for the Richards equation, it still involves solving large nonlinear algebraic equations. Accordingly, considerable efforts have been devoted to developing non-iterative semi-implicit methods for the Richards equation [30, 31, 34, 45], which convert implicit nonlinear problems into linear systems via linearization techniques. Paniconi et al. [45] demonstrated that non-iterative schemes appear as a promising alternative to iterative methods. Non-iterative implicit time-stepping schemes with adaptive truncation error control were developed by Kavetski et al. [30] for solving the pressure-head form of Richards equation. Keita et al. [31] proposed a linear semi-implicit second-order time-stepping method with a mixed finite element method, linearizing nonlinear terms via extrapolation formulas and Taylor approximations. It is evident that avoiding nonlinear iterations while allowing larger time steps constitutes a viable strategy for efficient temporal discretization, though further improvements in accuracy and stability remain desirable.

To improve existing works in achieving high-order accuracy, computational efficiency, and robustness, we consider a high-order explicit-implicit-null (EIN) time-marching scheme in this paper. This method was first proposed and applied by Douglas and Dupont [15] for nonlinear diffusion equations, and later formally named the EIN method by Duchemin and Eggers [16]. Recently, Tan et al. [53] developed a third-order EIN time-marching scheme for high-order dissipative and dispersive equations, coupled with spatial discretizations based on the FDM and LDG schemes. With the Fourier method, they performed a stability analysis for the simplified linear equations and offered guidance on coefficient selection. The basic idea of EIN method is to add and subtract a sufficiently large linear highest derivative term on one side of the considered equation (effectively adding zero), and then apply the IMEX time-marching method to the equivalent equation. That is, treat the added linear stiffness terms implicitly and all other terms explicitly. By appropriately choosing the coefficient of the added term, the scheme can be stable under a relaxed time step

restriction.

In this paper, we construct a third-order bound-preserving EIN-MRWENO scheme for the Richards equation in mass-conservative form (mixed or θ-based form). The time discretization adopts the EIN methodology, adding and subtracting a linear diffusion term on one side of the Richards equation. Since the linear added term is treated implicitly, only a linear system needs to be solved, and the time step can be relaxed to $\Delta t = O(h)$. Compared to other non-iterative semi-implicit methods, the EIN method offers a more intuitive theory and simpler implementation. For spatial discretization, we follow the design of [58], adopting a conservative MRWENO scheme in the finite difference framework. Specifically, a third-order MRWENO scheme is employed for the convection term, with the Roe speed being used to ensure correct upwind biasing and stability. For the nonlinear diffusion term, a fourth-order MRWENO scheme is used to tackle the degeneration issue, whereas the added linear term is discretized with a fourth-order central difference scheme. To enforce the physical bounds of numerical solutions, we adopt a simple BP sweeping technique that acts as a postprocessing step without compromising global conservation or accuracy. Over all grid points in a predefined order, a forward sweep and then a backward sweep are performed, where any value exceeding the bound is corrected together with its neighbor using the given positive weights and bound values. The discretization framework combining EIN and finite difference schemes offers simplicity in both algorithmic design and coding, along with efficiency benefits for 3D simulations, thereby facilitating direct integration into large-scale programmes. Numerical experiments, including benchmarks and 3D application infiltration cases, demonstrate the high-order accuracy, enhanced efficiency, BP performance, and broad applicability of the proposed method.

The outline of the paper unfolds as follows. After the introductory section, the governing equations and the hydraulic models are presented in Section 2. In Section 3, we describe the details of time and space discretizations, then elaborate on the procedure of the BP sweeping technique. Numerical tests are shown in Section 4. The last concluding section finalizes the paper.

2. Governing equations

2.1. Richards equation

The Richards equation, derived by combining the continuity equation with Darcy's law, describes the movement of unsteady unsaturated infiltration flow:

$$\frac{\partial \theta}{\partial t} - \nabla \cdot (K(\psi)\nabla\psi) + \frac{\partial K(\psi)}{\partial z} = 0, \tag{2.1}$$

where θ is moisture content, ψ is pressure head, K is hydraulic conductivity, z is the vertical coordinate taken positive downward and t is time. Eq. (2.1) is known as the mixed-form Richards equation. The Darcy flux is given by $\mathbf{q} = -K(\psi)\nabla H$, where H is the total head defined as $H = \psi - z$. With the chain rule of differentiation, the θ-based form is written as:

$$\frac{\partial \theta}{\partial t} - \nabla \cdot (D(\theta)\nabla\theta) + \frac{\partial K(\theta)}{\partial z} = 0, \tag{2.2}$$

and the ψ-based form is:

$$C(\psi)\frac{\partial \psi}{\partial t} - \nabla \cdot (K(\psi)\nabla\psi) + \frac{\partial K(\psi)}{\partial z} = 0, \tag{2.3}$$

where $C(\psi) = \partial\theta/\partial\psi$ is the specific fluid content function, and $D(\theta) = K(\theta)\partial\psi/\partial\theta = K(\theta)/C(\theta)$ is the fluid diffusivity function.

The mixed-form and θ-based equations offer advantages for constructing conservative numerical schemes, as they satisfy mass conservation intrinsically. Furthermore, the mixed form exhibits greater applicability to realistic complex media. We therefore focus on the numerical methods for the mixed-form equation (2.1) in the subsequent discussion.

2.2. Hydraulic models

For the solution of Richards equation, constitutive relations of hydraulic properties are required to characterize hydraulic conductivity K and moisture content θ as functions of pressure head ψ.

Several widely used hydraulic models are adopted in this work, one of which is the Van Genuchten-Mualem model [57]:

$$\begin{aligned} \theta_e &= \frac{\theta - \theta_r}{\theta_s - \theta_r} = (1 + (\alpha|\psi|)^n)^{-m}, \\ K &= K_s \theta_e^l \left(1 - \left(1 - \theta_e^{1/m}\right)^m\right)^2, \end{aligned} \tag{2.4}$$

where θ_r and θ_s are the residual and saturated moisture contents respectively, θ_e is the effective saturation ($0 \leq \theta_e \leq 1$), K_s is the saturated hydraulic conductivity, l is the pore connectivity index, usually taken as 0.5, α, n and m are empirical parameters and $m = 1 - 1/n$.

Another one is the Brooks-Corey model [9], which expresses the normalized moisture content θ_e as a power function of h:

$$\theta_e = \left(\frac{\psi}{\psi_b}\right)^{-\lambda}, \quad K = K_s \theta_e^{\eta}, \tag{2.5}$$

where ψ_b is the air-entry head value ($\psi \leq \psi_b \leq 0$), $\lambda > 0$ is the pore size distribution index, with typical values ranging between 0.1 and 10, and η is a model parameter.

Moreover, Gardner's exponential model [18], commonly employed for numerical validation, reads:

$$\theta_e = \exp(\rho\psi), \quad K = K_s \theta_e^{\beta}, \tag{2.6}$$

where ρ and β are model parameters.

3. Numerical methods

To implement the EIN method, we add and subtract a Laplacian operator with constant coefficient at one side of the mixed form Richards equation (2.1) for approximating the nonlinear diffusion term:

$$\frac{\partial \theta}{\partial t} = \underbrace{\nabla \cdot (K(\psi)\nabla\psi) - K(\psi)_z - a_1 \nabla^2 \theta}_{\mathcal{T}_1} + \underbrace{a_1 \nabla^2 \theta}_{\mathcal{T}_2}, \tag{3.1}$$

where a_1 is an appropriately large constant such that $\mathcal{T}_1$ is either not stiff, or less stiff and less dissipative compared to $\mathcal{T}_2$, thus it can be treated explicitly, and $\mathcal{T}_2$ is stiff and dissipative, thus will be discretized implicitly.

In this section, we will provide a specific description of the full spatial and temporal discretizations.

3.1. Spatial discretization

3.1.1. Discretization for the convection term

To achieve high order accuracy in space and control spurious oscillations near the wetting fronts, we adopt a third-order finite difference multi-resolution WENO (MRWENO) method to discretize the convection term, $K(\psi)_z$.

Take the one-dimensional (1D) case as an example. A uniform mesh z_i with constant mesh size $\Delta z = z_{i+1} - z_i$ is adopted for the computation, and the half point is denoted as $z_{i+1/2} = (z_i + z_{i+1})/2$. We construct a conservative flux difference to achieve the third-order accurate approximation at $z = z_i$, i.e.,

$$\frac{\partial K(\psi)}{\partial z}\Big|_{z_i} = \frac{\hat{K}_{i+1/2} - \hat{K}_{i-1/2}}{\Delta z} + O(\Delta z^3),$$

where $\hat{K}_{i\pm1/2}$ is the numerical flux obtained by the MRWENO reconstruction, and the set of grid points $S = \{z_{i-p}, ..., z_{i+q}\}$ involved in the flux approximation constitutes the stencil.

In order to ensure correct upwind biasing and stability, the Roe speed is utilized instead of the flux splitting used in [68] to avoid the singularity arising from K'. The characteristic direction for the mixed form equation (2.1) is given by $K'(\psi)\psi'(\theta)$, and the Roe speed is defined as

$$\bar{a}_{i+1/2} = \left(K(\psi_{i+1}) - K(\psi_i)\right)\left(\psi_{i+1} - \psi_i\right)\left(\psi(\theta_{i+1}) - \psi(\theta_i)\right)\left(\theta_{i+1} - \theta_i\right).$$

Here and hereafter, we let ψ_i and θ_i be the point values of ψ and θ at the grid point z_i, let $K_i = K(\psi_i)$ and denote the interval $I_i = [z_{i-1/2}, z_{i+1/2}]$. The third-order MRWENO reconstruction to obtain the numerical flux $\hat{K}_{i+1/2}$ follows a similar procedure to that in our recent work [58], and is briefly summarized as follows for completeness.

1. Select two nested central spatial stencils $S^{(0)} = \{I_i\}$ and $S^{(1)}$ that depends on the Roe speed. Specifically, if $\bar{a}_{i+1/2} \geq 0$, indicating flow from left to right, the left-biased stencil $S^{(1)} =$

$\{I_{i-1}, I_i, I_{i+1}\}$ is employed; otherwise, the right-biased stencil $S^{(1)} = \{I_i, I_{i+1}, I_{i+2}\}$ is used.

Reconstruct a zeroth degree polynomial $q_0(z)$ and a quadratic polynomial $q_1(z)$ which satisfy

$$\frac{1}{\Delta z}\int_{z_j-\Delta z/2}^{z_j+\Delta z/2} q_k(z)dz = \frac{K_j}{K_M},\ z_j \in S^{(k)}, \quad k = 0, 1,$$

where $K_M = \max\{|K_j| : z_j \in S^{(1)}\} + \epsilon_0$ is a scaling factor, with $\epsilon_0 = 10^{-40}$ used to avoid division by zero. The introduction of K_M serves to normalize the values within the stencil, effectively alleviating the adverse effects of extreme numerical scales induced by the nonlinearity of Richards equation on the WENO reconstruction, thereby improving numerical stability.

2. Obtain equivalent expressions for the reconstruction polynomials. We denote $p_0(z) = q_0(z)$ and

$$p_1(z) = \frac{1}{\gamma_1}q_1(z) - \frac{\gamma_0}{\gamma_1}p_0(z),$$

where γ_0 and γ_1 are linear weights that can be any positive numbers as long as $\gamma_0 + \gamma_1 = 1$ and $\gamma_1 \neq 0$.

3. Compute the smoothness indicators β_0 and β_1, which measures how smooth the functions $p_0(z)$ and $p_1(z)$ are in the interval $[z_{i-1/2}, z_{i+1/2}]$. The smoothness indicator β_1 is defined as

$$\beta_1 = \sum_{\alpha=1}^{2}\int_{z_i-\Delta z/2}^{z_i+\Delta z/2} \Delta z^{2\alpha-1}\left(\frac{d^\alpha p_1(z)}{dz^\alpha}\right)^2 dz,$$

while β_0 is defined as follows:

$$\varsigma_0 = \left(\frac{K_i}{K_M} - \frac{K_{i-1}}{K_M}\right)^2, \quad \varsigma_1 = \left(\frac{K_{i+1}}{K_M} - \frac{K_i}{K_M}\right)^2,$$

$$\bar{\gamma}_{0,1} = \begin{cases} 1, & \varsigma_0 \geq \varsigma_1, \\ 10, & \text{otherwise}, \end{cases} \qquad \bar{\gamma}_{1,1} = 11 - \bar{\gamma}_{0,1}$$

$$\tilde{\gamma}_{0,1} = \frac{\bar{\gamma}_{0,1}}{\bar{\gamma}_{0,1} + \bar{\gamma}_{1,1}}, \quad \tilde{\gamma}_{1,1} = 1 - \tilde{\gamma}_{0,1},$$

$$\sigma_0 = \tilde{\gamma}_{0,1}\left(1 + \frac{|\varsigma_0 - \varsigma_1|^r}{\varsigma_0 + \varepsilon}\right), \quad \sigma_1 = \tilde{\gamma}_{1,1}\left(1 + \frac{|\varsigma_0 - \varsigma_1|^r}{\varsigma_1 + \varepsilon}\right), \quad \sigma = \sigma_0 + \sigma_1,$$

where ε is a small positive number to avoid the denominator to become zero, e.g. $\varepsilon = 10^{-10}$. Then we set

$$\beta_0 = \frac{1}{\sigma^2}\left(\sigma_0\left(\frac{K_i}{K_M} - \frac{K_{i-1}}{K_M}\right) + \sigma_1\left(\frac{K_{i+1}}{K_M} - \frac{K_i}{K_M}\right)\right)^2.$$

4. Compute the nonlinear weights based on the linear weights and the smoothness indicators. The nonlinear weights are given as

$$\omega_k = \frac{\bar{\omega}_k}{\bar{\omega}_0 + \bar{\omega}_1}, \quad \bar{\omega}_k = \gamma_k\left(1 + \frac{\tau}{\varepsilon + \beta_k}\right), \ k = 0, 1,$$

where $\tau = |\beta_1 - \beta_0|$.

5. The new final reconstruction polynomial $w_i(z)$ is given by

$$w_i(z) = K_M\left(\omega_0 p_0(z) + \omega_1 p_1(z)\right),$$

and the numerical flux $\hat{K}_{i+1/2}$ is obtained by setting $\hat{K}_{i+1/2} = w_i(z_{i+1/2})$.

The algorithm for the high-dimensional version is implemented in a dimension by dimension fashion. For the convection term $K(\psi)_z$, we simply fix the x- and y-indices and perform the same 1D operation along the z-direction, which is omitted here.

3.1.2. Discretization for the nonlinear diffusion term

For the approximation of the nonlinear diffusion term $\nabla \cdot (K(\psi)\nabla\psi)$, a fourth-order finite difference MRWENO scheme is adopted to overcome potential degeneracy issues.

We first consider the 1D case, and denote the flux function $G(\psi) := K(\psi)\frac{\partial \psi}{\partial z}$. The conservative finite difference approximation of the diffusion term then reads

$$\frac{\partial G(\psi)}{\partial z}\Big|_{z_i} = \frac{\hat{G}_{i+1/2} - \hat{G}_{i-1/2}}{\Delta z} + O(\Delta z^4),$$

where $\hat{G}_{i\pm1/2}$ is the numerical flux at the interface $z_{i\pm1/2}$. To reconstruct $\hat{G}_{i+1/2}$, we first approximate the derivative $\frac{\partial \psi}{\partial z}$ at z_i by

$$\frac{\partial \psi}{\partial z}\Big|_{z_i} = \frac{\hat{\psi}_{i+1/2} - \hat{\psi}_{i-1/2}}{\Delta z} + O(\Delta z^4),$$

and we have

$$G_i = K(\psi_i)\frac{\hat{\psi}_{i+1/2} - \hat{\psi}_{i-1/2}}{\Delta z},$$

which serve as a fourth-order accurate approximation of $G(\psi(z_i))$. Therefore, we require two MRWENO reconstruction procedures to approximate $\hat{\psi}_{i+1/2}$ and $\hat{G}_{i+1/2}$, respectively.

The fourth-order MRWENO program follows a similar framework as in Section 3.1.1, with K_j replaced by ψ_j and G_j, respectively. The only difference is the stencils, which are fully symmetric about the interface $z_{i+1/2}$, as the diffusion exhibits no upwind bias. That is,

$$S_{\psi}^{(0)} = \{I_{i+1}\},\ S_{G}^{(0)} = \{I_i\},\ S^{(1)} = \{I_i, I_{i+1}\},\ S^{(2)} = \{I_{i-1}, I_i, I_{i+1}, I_{i+2}\},$$

where $S_{\psi}^{(0)}$ and $S_{G}^{(0)}$ denote the zeroth-degree stencil $S^{(0)}$ used in the reconstruction of $\hat{\psi}_{i+1/2}$ and $\hat{G}_{i+1/2}$, respectively. For more details about the MRWENO reconstruction procedure to obtain the numerical fluxes $\hat{\psi}_{i+1/2}$ and $\hat{G}_{i+1/2}$, we refer to [58, 68].

We further consider the two-dimensional (2D) version. A uniform mesh (x_k, z_i) is utilized, with constant mesh sizes $\Delta x = x_{k+1} - x_k$ and $\Delta z = z_{i+1} - z_i$. The half points are denoted as $x_{k+1/2} = \frac{1}{2}(x_k + x_{k+1})$, $z_{i+1/2} = \frac{1}{2}(z_i + z_{i+1})$. Denote $F(\psi) := K(\psi)\frac{\partial \psi}{\partial x}$, and the fourth-order conservative difference schemes are formulated as

$$\begin{aligned}
\frac{\partial \psi}{\partial x}\Big|_{(x_k,z_i)} &= \frac{\hat{\psi}_{k+1/2,i} - \hat{\psi}_{k-1/2,i}}{\Delta x} + O(\Delta x^4),\\
\frac{\partial F(\psi)}{\partial x}\Big|_{(x_k,z_i)} &= \frac{\hat{F}_{k+1/2,i} - \hat{F}_{k-1/2,i}}{\Delta x} + O(\Delta x^4),
\end{aligned}$$

and

$$\frac{\partial \psi}{\partial z}\Big|_{(x_k,z_i)} = \frac{\hat{\psi}_{k,i+1/2} - \hat{\psi}_{k,i-1/2}}{\Delta z} + O(\Delta z^4),$$
$$\frac{\partial G(\psi)}{\partial z}\Big|_{(x_k,z_i)} = \frac{\hat{G}_{k,i+1/2} - \hat{G}_{k,i-1/2}}{\Delta z} + O(\Delta z^4),$$

where F and G are approximated at the grid points by

$$F_{k,i} = K(\psi_{k,i})\frac{\hat{\psi}_{k+1/2,i} - \hat{\psi}_{k-1/2,i}}{\Delta x}, \quad G_{k,i} = K(\psi_{k,i})\frac{\hat{\psi}_{k,i+1/2} - \hat{\psi}_{k,i-1/2}}{\Delta z}.$$

The numerical fluxes $\hat{\psi}_{k\pm1/2,i}$, $\hat{F}_{k\pm1/2,i}$ and $\hat{\psi}_{k,i\pm1/2}$, $\hat{G}_{k,i\pm1/2}$ are obtained by the above reconstruction algorithm.

The procedure for 3D case is applied in the same manner and is therefore omitted.

3.1.3. Discretization for the linear diffusion term

The added linear diffusion term $\nabla^2\theta$ can be approximated by a standard fourth order central difference scheme, for example, in 1D space:

$$\frac{\partial^2 \theta}{\partial z^2}\Big|_{z_i} = \frac{\hat{D}_{i+1/2} - \hat{D}_{i-1/2}}{\Delta z} + O(\Delta z^4),$$

with

$$\hat{D}_{i+1/2} = \frac{-\theta_{i+2} + 15\theta_{i+1} - 15\theta_i + \theta_{i-1}}{12\Delta z}.$$

The discretization extends similarly to 2D and 3D cases, with additional details simplified for brevity.

Remark 3.1. *The spatial discretization described above achieves global third-order accuracy, and arbitrarily high-order accuracy can be attained by employing wider stencils, as demonstrated in [58, 68]. Furthermore, the proposed method is constructed within a conservative discretization framework, which enables its direct application to the θ-based form Richards equation (2.2) with straightforward extensibility. The discussions and results are available in [58].*

3.2. EIN temporal discretization

Assume that the semi-discrete scheme of (3.1) is written in the form of a first order ODE system

$$\frac{d\theta}{dt} = \mathcal{N}(t, \psi, \theta) + \mathcal{L}(t, \psi, \theta), \tag{3.2}$$

where $\mathcal{N}(t, \psi, \theta)$ and $\mathcal{L}(t, \psi, \theta)$ arise from the spatial discretization of the two parts $\mathcal{T}_1$ and $\mathcal{T}_2$ in (3.1), respectively. To solve (3.2), a third order IMEX Runge-Kutta method [3] is used. Let θ^n and ψ^n denote the numerical solutions at time t^n, the time-marching method to find θ^{n+1} and ψ^{n+1} is given by

$$\begin{cases} \theta^{(m)} = \theta^n + \Delta t \sum_{l=1}^{m} \tilde{a}_{ml} \mathcal{L}(t_l^n, \psi^{(l)}, \theta^{(l)}) + \Delta t \sum_{l=1}^{m-1} \hat{a}_{ml} \mathcal{N}(t_l^n, \psi^{(l)}, \theta^{(l)}), \\ \psi^{(m)} = \psi(\theta^{(m)}), \quad 1 \le m \le 5, \end{cases} \tag{3.3}$$

$$\begin{cases} \theta^{n+1} = \theta^n + \Delta t \sum_{l=1}^{5} \tilde{b}_l \mathcal{L}(t_l^n, \psi^{(l)}, \theta^{(l)}) + \Delta t \sum_{l=1}^{5} \hat{b}_l \mathcal{N}(t_l^n, \psi^{(l)}, \theta^{(l)}), \\ \psi^{n+1} = \psi(\theta^{n+1}), \end{cases} \tag{3.4}$$

where $\theta^{(m)}$ and $\psi^{(m)}, 1 \le m \le 5$ are intermediate values approximating $\theta(t_m^n)$ and $\psi(t_m^n)$, respectively, with

$$t_m^n = t^n + c_m \Delta t, \quad c_m = \sum_{l=1}^{m} \tilde{a}_{ml} = \sum_{l=1}^{m-1} \hat{a}_{ml}.$$

Denote the matrices $(\tilde{a}_{ml})_{5\times5}$ and $(\hat{a}_{ml})_{5\times5}$, and coefficient vectors $(\tilde{b}_1, ..., \tilde{b}_5)$, $(\hat{b}_1, ..., \hat{b}_5)$, and $(c_1, ..., c_5)$, then we can express the IMEX Runge-Kutta method as the following Butcher tableau:

	$\tilde{a}_{ml}$					c_m	$\hat{a}_{ml}$					
$m \diagdown l$	1	2	3	4	5	-	1	2	3	4	5	$l \diagdown m$
1	0	0	0	0	0	0	0	0	0	0	0	1
2	0	$\frac{1}{2}$	0	0	0	$\frac{1}{2}$	$\frac{1}{2}$	0	0	0	0	2
3	0	$\frac{1}{6}$	$\frac{1}{2}$	0	0	$\frac{2}{3}$	$\frac{11}{18}$	$\frac{1}{18}$	0	0	0	3
4	0	$-\frac{1}{2}$	$\frac{1}{2}$	$\frac{1}{2}$	0	$\frac{1}{2}$	$\frac{5}{6}$	$-\frac{5}{6}$	$\frac{1}{2}$	0	0	4
5	0	$\frac{3}{2}$	$-\frac{3}{2}$	$\frac{1}{2}$	$\frac{1}{2}$	1	$\frac{1}{4}$	$\frac{7}{4}$	$\frac{3}{4}$	$-\frac{7}{4}$	0	5
$\tilde{b}_l$	0	$\frac{3}{2}$	$-\frac{3}{2}$	$\frac{1}{2}$	$\frac{1}{2}$	-	$\frac{1}{4}$	$\frac{7}{4}$	$\frac{3}{4}$	$-\frac{7}{4}$	0	$\hat{b}_l$

Next, it remains to determine the coefficient of the added linear Laplacian operator, i.e., the constant a_1 in (3.1), which we denote as

$$a_1 = a_0 \times \max_{\theta} |D(\theta)| = a_0 \times \gamma_D, \quad \gamma_D = \max_{\psi} |K(\psi)/C(\psi)|, \tag{3.5}$$

where a_0 is a stability parameter, whose exact lower bound is crucial for the robustness and resolution of the simulation. With the aid of Fourier method, a stability analysis for the proposed scheme can be conducted, and the range of a_0 can be derived numerically. The detailed results are available in [53, 54] for the convection-diffusion equations, which concludes that $a_0 \geq 0.54$. A smaller a_0 cannot guarantee the stability, while a larger a_0 also introduces excessive error. Thus, $a_0 = 0.54$ is a preferred choice, ensuring stability while relaxing the time step to

$$\Delta t = \frac{C_u}{\gamma_C} \Delta z, \quad \gamma_C = \max_{\psi} |K'(\psi)/C(\psi)|, \tag{3.6}$$

where C_u is the Courant number.

Remark 3.2. *In general, the Courant number C_u is taken as a constant not exceeding 1, as detailed in the stability analysis results in [53, 54]. However, for some cases with strong nonlinearities—such as sharp fronts driven by boundary conditions and highly heterogeneous soils—the scheme may require a larger a_1 or a smaller time step to ensure stability. This results in smaller and case-dependent values of C_u in the numerical experiments section, which also reflects the high stiffness of these problems.*

3.3. Bound-preserving sweeping technique

To guarantee the physical admissibility of the numerical solution $\theta \in [\theta_r, \theta_s]$, we introduce a conservative bound-preserving sweeping technique. Take the 1D case as an example. We define the weighted average $\bar{\Theta} = \frac{1}{N}\sum_{i=1}^{N}\theta_i$, where $N = L/\Delta z$ is the number of grid points and L is the domain length. The conservative flux-difference form of our scheme ensures that $\bar{\Theta}$ is discretely conserved. Consequently, provided the initial condition and boundary values lie within the physically admissible range, it follows that $\bar{\Theta} \in [\theta_r, \theta_s]$. More precisely, for periodic or no-flux boundary conditions, the numerical solution obeys a strict maximum principle, that is, $\theta_i^n \in [\theta_m, \theta_M]$ for all i and $n \geq 0$, with $\theta_m = \min_i\{\theta_i^0\}$ and $\theta_M = \max_i\{\theta_i^0\}$. Henceforth, we denote the minimum and maximum bounds to be preserved by θ_m and θ_M, respectively. The detailed procedure consists of a forward sweep followed up by a backward sweep, as outlined below.

Algorithm 1 Bound-preserving sweeping procedure

Require: A set of numerical point values $\{\theta_i\}_{i=1}^N$ (which do not necessarily lie in $[\theta_r, \theta_s]$); and the weighted average $\bar{\Theta} \in [\theta_r, \theta_s]$.

Ensure: The updated $\theta_i \in [\theta_r, \theta_s]$, $\forall i$, and $\bar{\Theta}$ remains unchanged.

1. Forward Sweep
for $i = 1$ **to** $N - 1$ **do**
  if $\theta_i < \theta_m$ **then**
    $\theta_{i+1} \leftarrow \theta_{i+1} + (\theta_i - \theta_m), \quad \theta_i \leftarrow \theta_m;$
  end if
  if $\theta_i > \theta_M$ **then**
    $\theta_{i+1} \leftarrow \theta_{i+1} + (\theta_i - \theta_M), \quad \theta_i \leftarrow \theta_M.$
  end if
end for
2. Backward Sweep
for $i = N$ **to** 2 **do**
  if $\theta_i < \theta_m$ **then**
    $\theta_{i-1} \leftarrow \theta_{i-1} + (\theta_i - \theta_m), \quad \theta_i \leftarrow \theta_m;$
  end if
  if $\theta_i > \theta_M$ **then**
    $\theta_{i-1} \leftarrow \theta_{i-1} + (\theta_i - \theta_M), \quad \theta_i \leftarrow \theta_M.$
  end if
end for

The sweeping procedure is applied as a post-processing step at the time step t^n and intermediate stage t_m^n to guarantee the bound-preserving property and global conservation, without depending

on the underlying space-time discretisation scheme. For the supporting theorems and proofs, we refer the reader to [38]. Furthermore, the numerical accuracy is also verified by the tests in Section 4.

For the 2D case, the weighted average is defined as $\bar{\Theta} = \frac{1}{N_x N_z} \sum_{k=1}^{N_x} \sum_{i=1}^{N_z} \theta_{k,i}$. We treat the numerical solutions $\{\theta_{k,i}\}_{k,i=1}^{N_x N_z}$ as a one dimensional matrix, thereby enabling the application of Algorithm 1. The sweeping orders are varied, while attempting to maintain the neighboring relations of the points. There are two orders with comparable sweeping effects:

- Column by column: $\{\theta_{1,1}, ..., \theta_{N,1}, \theta_{N,2}, ..., \theta_{1,2}, \theta_{1,3}...\}$. For each column $i = 1, 2, ..., N_z$, perform the sweeping procedure with order $k = 1, 2, ..., N_x$ for odd i, and with order $k = N_x, N_x - 1, ..., 1$ for even i.

- Row by row: $\{\theta_{1,1}, ..., \theta_{1,N}, \theta_{2,N}, ..., \theta_{2,1}, \theta_{3,1}...\}$. For each row $k = 1, 2, ..., N_x$, perform the sweeping procedure with order $i = 1, 2, ..., N_z$ for odd k, and with order $i = N_z, N_z - 1, ..., 1$ for even k.

We can use either of these orders to sweep, and other suitable orders are also admissible. The 3D case is processed in the same manner.

4. Numerical experiments

This section is devoted to the numerical tests and simulations of the bound-preserving EIN-MRWENO scheme developed in the preceding sections. The examples are arranged in order of increasing dimension and complexity. A uniform grid spacing is adopted in each spatial direction for all test cases, which we denote by h.

To show the efficiency of the EIN scheme, we compare the computational costs and accuracy with the explicit three-stage third-order strong stability preserving (SSP) Runge-Kutta (RK)

method. The form of the SSP-RK3 method for solving the ODE system $d\theta/dt = L(\psi)$ are

$$\begin{cases} \theta^{(1)} = \theta^n + \Delta t L\left(\psi^n\right), \\ \psi^{(1)} = \psi(\theta^{(1)}); \\ \theta^{(2)} = \theta^n + \Delta t \left(\frac{1}{4}L(\psi^n) + \frac{1}{4}L(\psi^{(1)})\right), \\ \psi^{(2)} = \psi(\theta^{(2)}); \\ \theta^{n+1} = \theta^n + \Delta t \left(\frac{1}{6}L(\psi^n) + \frac{1}{6}L(\psi^{(1)}) + \frac{2}{3}L(\psi^{(2)})\right), \\ \psi^{n+1} = \psi(\theta^{n+1}). \end{cases}$$

For the EIN scheme, the time step size is chosen according to (3.6). For the SSP-RK3 scheme, we follow the CFL stability condition, taking $\Delta t = \frac{C_u}{\gamma_C/\Delta z + \gamma_D/\Delta z^2}$ for 1D problems, $\Delta t = \frac{C_u}{\gamma_C/\Delta z + \gamma_D/\Delta x^2 + \gamma_D/\Delta z^2}$ for 2D problems, and $\Delta t = \frac{C_u}{\gamma_C/\Delta z + \gamma_D/\Delta x^2 + \gamma_D/\Delta y^2 + \gamma_D/\Delta z^2}$ for 3D problems. Unless otherwise stated, the Courant number is taken as $C_u = 0.4$. Additionally, a summary of the efficiency comparison for the test cases is provided in Section 4.3.

4.1. Numerical verification

Example 4.1. *Accuracy and efficiency test*

In this test, we solve the mixed-form Richards equation with artificial source terms on domains $[0, 2\pi]^d$ under periodic boundary conditions, where $d = 1, 2, 3$ are the dimensions. The three different hydraulic models presented in Section 2.2 are tested with the parameters:

$$\theta_r = 0,\ \theta_s = 1,\ \alpha = 1,\ K_s = 1,\ n = 2,\ m = \frac{1}{2},\ \psi_b = -1,\ \lambda = 10,\ \eta = \frac{1}{10},\ \rho = 1,\ \beta = 1,$$

and we have

- Van Genuchten-Mualem model: $K(\psi) = (1+\psi^2)^{-1/4}(1 - \sqrt{1-(1+\psi^2)^{-1}})^2$, $\psi(\theta) = -\sqrt{\theta^{-2}-1}$,
- Brooks-Corey model: $K(\psi) = -1/\psi$, $\psi(\theta) = -\theta^{-1/10}$,

- Gardner model: $K(\psi) = \exp(\psi),\ \psi(\theta) = \log\theta,$

The exact solutions of the problem are given as $\theta(z,t) = \frac{1}{2}+\frac{1}{6}\sin(z-t)$, $\theta(x,z,t) = \frac{1}{2}+\frac{1}{6}\sin(x+z-t)$ and $\theta(x,y,z,t) = \frac{1}{2}+\frac{1}{6}\sin(x+y+z-t)$ for $d = 1,2,3$ respectively, which are smooth and do not exceed the bounds of $[\theta_r, \theta_s]$. The source terms S can be derived accordingly and are available in [58].

We test the EIN and SSP-RK3 schemes coupled with the third-order MRWENO spatial discretization by setting the final time to $T = 1$. The errors, numerical orders of accuracy, and the CPU times are shown in Tables 1 to 3 for $d = 1,2,3$. We can observe that the schemes achieve the designed order of accuracy for different hydraulic models in 1D, 2D and 3D, respectively. Furthermore, the CPU time required by the EIN-MRWENO scheme is significantly lower than that of the SSPRK-MRWENO scheme, with the savings scaling proportionally to the grid size. For highly refined meshes, the reduction in computational cost can reach up to 99%.

Example 4.2. *Bound-preserving sweeping test*

This example is designed to demonstrate the effectiveness of the BP sweeping technique while maintaining the accuracy of the proposed EIN-MRWENO discretization. The Gardner model (2.6) is employed to describe the hydraulic properties of the Richards equation, with parameters $\theta_r = 0$, $\theta_s = 1$, $\rho = 1$, $\beta = 1$, and $K_s = 10^4$, yielding the constitutive relations $\psi(\theta) = \log\theta$ and $K(\psi) = 10^4 e^h$. Periodic boundary conditions are imposed on the domain $z \in [0, 10^4]$, and the initial condition is prescribed as $\theta(z,0) = \frac{1}{2} + \frac{1}{2}\left(1 - ((1+\sin(2\pi z/10^4))/2)^4\right)^4$. The solution θ evolves within the range $\theta_m = 1/2$ and $\theta_M = 1$, which corresponds to the bounds to be preserved by the sweeping procedure. A reference solution is computed on a fine mesh of 2560 grid points at $T = 1$. The errors and convergence orders, both without and with BP sweeping, are reported in Table 4. Negative values of $\theta_{\min} - \theta_m$ and $\theta_M - \theta_{\max}$ imply the approximation has gone out of the bound $[\theta_m, \theta_M]$. And BP(%) in the table represents the percentage of grid points whose values are adjusted during the sweeping process. We can clearly see that the sweeping technique effectively enforces the bound-preserving property, while the designed order of accuracy is preserved.

Table 1. Numerical accuracy and comparison of efficiency in 1D space of Example 4.1.

Van Genuchten-Mualem model								
	EIN-MRWENO			SSPRK-MRWENO				
Grid	L_1 error	Order	CPU time	L_1 error	Order	CPU time	Ratio	Savings(%)
80	5.39E-06	-	0.027	4.30E-06	-	0.124	4.59	78.20
160	5.84E-07	3.21	0.098	5.15E-07	3.06	0.600	6.09	83.59
320	6.93E-08	3.07	0.402	6.47E-08	2.99	3.639	9.05	88.94
640	7.90E-09	3.13	1.823	7.97E-09	3.02	17.020	9.34	89.29
1280	8.42E-10	3.23	11.754	7.64E-10	3.38	122.463	10.42	90.40
Brooks-Corey model								
	EIN-MRWENO			SSPRK-MRWENO				
Grid	L_1 error	Order	CPU time	L_1 error	Order	CPU time	Ratio	Savings(%)
80	4.41E-06	-	0.041	2.58E-06	-	0.093	2.28	56.09
160	4.60E-07	3.26	0.061	2.57E-07	3.33	0.353	5.83	82.84
320	5.20E-08	3.14	0.134	2.14E-08	3.59	2.087	15.60	93.59
640	6.26E-09	3.05	0.710	2.25E-09	3.25	9.916	13.97	92.84
1280	7.70E-10	3.02	5.651	2.63E-10	3.10	114.301	20.23	95.06
Gardner model								
	EIN-MRWENO			SSPRK-MRWENO				
Grid	L_1 error	Order	CPU time	L_1 error	Order	CPU time	Ratio	Savings(%)
80	5.22E-06	-	0.048	6.66E-06	-	0.157	3.26	69.29
160	5.74E-07	3.19	0.088	6.45E-07	3.37	0.658	7.49	86.66
320	6.75E-08	3.09	0.402	9.41E-08	2.78	4.094	10.19	90.18
640	7.36E-09	3.20	2.705	7.05E-09	3.74	26.233	9.70	89.69
1280	8.74E-10	3.07	19.828	8.43E-10	3.07	257.979	13.01	92.31

4.2. Application cases

Example 4.3. *1D infiltration problem for validation*

We consider a one-dimensional infiltration problem that possesses a simplified analytical solution, providing a benchmark for numerical validation. It was originally proposed by Basha [5] based on Gardner's exponential model (2.6) and has been employed in [25, 41]. The soil parameters are given by

$$\theta_r = 0.0286,\ \theta_s = 0.3658,\ K_s = 0.2254\,\text{cm/min},\ \beta = 1.$$

The parameter ρ (cm^{-1}) can be interpreted as a measure of the relative importance of advection

Table 2. Numerical accuracy and comparison of efficiency in 2D space of Example 4.1.

Van Genuchten-Mualem model								
	EIN-MRWENO			SSPRK-MRWENO				
Grid	L_1 error	Order	CPU time	L_1 error	Order	CPU time	Ratio	Savings(%)
40×40	3.17E-05	-	0.284	2.32E-05	-	0.989	3.48	71.24
80×80	3.86E-06	3.04	1.601	3.11E-06	2.90	9.113	5.69	82.43
160×160	4.37E-07	3.14	8.933	3.69E-07	3.08	117.168	13.12	92.38
320×320	5.19E-08	3.07	36.352	5.01E-08	2.88	1587.201	43.66	97.71
640×640	6.00E-09	3.11	204.510	6.22E-09	3.01	17262.651	84.41	98.82
Brooks-Corey model								
	EIN-MRWENO			SSPRK-MRWENO				
Grid	L_1 error	Order	CPU time	L_1 error	Order	CPU time	Ratio	Savings(%)
40×40	3.74E-05	-	0.132	1.42E-05	-	0.985	7.45	86.57
80×80	4.23E-06	3.15	0.492	1.94E-06	2.87	7.745	15.74	93.65
160×160	4.92E-07	3.10	2.660	1.75E-07	3.47	84.199	31.65	96.84
320×320	5.64E-08	3.12	18.861	1.47E-08	3.57	1010.379	53.57	98.13
640×640	6.80E-09	3.05	84.308	1.72E-09	3.10	19498.926	231.28	99.57
Gardner model								
	EIN-MRWENO			SSPRK-MRWENO				
Grid	L_1 error	Order	CPU time	L_1 error	Order	CPU time	Ratio	Savings(%)
40×40	3.01E-05	-	0.389	2.93E-05	-	3.234	8.32	87.98
80×80	3.60E-06	3.06	1.683	5.09E-06	2.52	26.956	16.02	93.76
160×160	4.06E-07	3.15	9.345	5.10E-07	3.32	311.403	33.32	97.00
320×320	4.84E-08	3.07	63.199	7.04E-08	2.86	3609.670	57.12	98.25
640×640	5.23E-09	3.21	272.892	4.96E-09	3.83	41812.506	153.22	99.35

(gravity) compared to diffusion (capillarity). We define the constant celerity c and diffusivity D,

$$c = \frac{\partial K}{\partial \theta} = \frac{K_s}{\theta_s - \theta_r}, \quad D = K(\theta)\frac{\partial \psi}{\partial \theta} = \frac{K_s}{\rho(\theta_s - \theta_r)}.$$

The following two distinct regimes are considered:

(1) Convection-dominated problem:

$$\theta(z,t) = \frac{\theta_0 - \theta_I}{2}\left[E_{-1} + \exp(cz/D)E_{+1}\right] + \theta_I, \quad E_{\pm 1} = \operatorname{erfc}\left(\frac{z \pm ct}{2\sqrt{Dt}}\right),$$

$$\theta(0,t) = \theta_0 = 0.3, \quad \theta(z,0) = \theta_I = 0.03, \quad \rho = 1.0\,\mathrm{cm}^{-1}.$$

Table 3. Numerical accuracy and comparison of efficiency in 3D space of Example 4.1.

Van Genuchten-Mualem model								
	EIN-MRWENO			SSPRK-MRWENO				
Grid	L_1 error	Order	CPU time	L_1 error	Order	CPU time	Ratio	Savings(%)
10×10×10	4.99E-03	-	0.304	1.52E-03	-	1.286	4.23	76.36
20×20×20	5.19E-04	3.26	1.470	1.88E-04	3.01	6.369	4.33	76.91
40×40×40	2.96E-05	4.13	7.585	1.90E-05	3.31	43.064	5.68	82.39
80×80×80	3.26E-06	3.18	51.370	2.62E-06	2.86	629.824	12.26	91.84
160×160×160	3.77E-07	3.11	662.587	2.98E-07	3.14	16839.287	25.41	96.07
Brooks-Corey model								
	EIN-MRWENO			SSPRK-MRWENO				
Grid	L_1 error	Order	CPU time	L_1 error	Order	CPU time	Ratio	Savings(%)
10×10×10	1.46E-03	-	0.243	1.13E-03	-	1.406	5.78	82.71
20×20×20	2.22E-04	2.71	0.843	9.63E-05	3.55	7.993	9.49	89.46
40×40×40	3.27E-05	2.76	4.279	1.10E-05	3.12	69.843	16.32	93.87
80×80×80	4.25E-06	2.94	26.391	1.67E-06	2.72	727.947	27.58	96.37
160×160×160	5.36E-07	2.99	323.834	1.43E-07	3.55	17792.290	54.94	98.18
Gardner model								
	EIN-MRWENO			SSPRK-MRWENO				
Grid	L_1 error	Order	CPU time	L_1 error	Order	CPU time	Ratio	Savings(%)
10×10×10	2.65E-03	-	0.573	2.17E-03	-	8.883	15.49	93.54
20×20×20	3.53E-04	2.91	2.840	2.31E-04	3.23	50.003	17.60	94.32
40×40×40	1.97E-05	4.16	13.148	1.80E-05	3.69	307.268	23.37	95.72
80×80×80	2.78E-06	2.83	86.824	5.36E-06	1.74	2630.210	30.29	96.70
160×160×160	3.20E-07	3.12	964.185	4.25E-07	3.66	54234.192	56.25	98.22

where erfc(·) is the complementary error function, defined as $\mathrm{erfc}(x) = 2/\sqrt{\pi}\int_x^\infty \exp(-\omega^2)d\omega$.

(2) Diffusion-dominated problem:

$$\theta(z,t) = \theta_I - \frac{q(\theta_s-\theta_r)}{2K_s}\left[E_{-1} - \left(1+\frac{cz}{D}+\frac{c^2t}{D}\right)\exp(cz/D)E_{+1} + 2c\sqrt{\frac{t}{\pi D}}\exp\left(\frac{cz}{2D}-\frac{c^2t}{4D}-\frac{z^2}{4Dt}\right)\right],$$

$$-K(\psi(0,t))\left(\frac{\partial\psi(0,t)}{\partial z}-1\right) = q = -0.15\,\mathrm{cm/min},$$

$$\theta(z,0) = \theta_I = \theta_r + \epsilon_I, \quad \rho = 0.025\,\mathrm{cm}^{-1},$$

where a small value $\epsilon_I = 10^{-5}$ is introduced to avoid the singularity in the pressure head $\psi(\theta) = 1/\rho \ln\theta_e$, ensuring the initial condition is well-defined.

Table 4. Numerical errors and orders of Example 4.2 without and with BP sweeping

	Grid	L_1 error	Order	L^∞ error	Order	BP(%)	$\theta_{\min} - \theta_m$	$\theta_M - \theta_{\max}$
Without BP sweeping	40	5.95E-03	-	3.05E-02	-	-	2.56E-03	7.21E-05
	80	2.18E-03	1.45	1.29E-02	1.24	-	2.12E-05	-1.23E-05
	160	2.35E-04	3.22	8.68E-04	3.89	-	-4.41E-05	-5.38E-06
	320	3.16E-05	2.89	1.18E-04	2.88	-	-1.70E-06	-4.88E-08
	640	4.01E-06	2.98	1.49E-05	2.98	-	6.91E-08	1.10E-09
With BP sweeping	40	5.66E-03	-	1.97E-02	-	1.54	2.16E-03	7.87E-05
	80	2.31E-03	1.30	1.38E-02	0.51	11.25	0	0
	160	2.56E-04	3.17	1.17E-03	3.57	17.82	0	0
	320	3.16E-05	3.02	1.18E-04	3.31	11.25	0	0
	640	4.01E-06	2.98	1.49E-05	2.98	1.68	6.95E-08	1.11E-09

Figure 1 presents the numerical solutions for the convection-dominated and diffusion-dominated problems at various times, which are in good agreement with the analytical solutions. As time advances, the wetting fronts propagate downward. For convection-dominated case, infiltration is rapid and gravity-driven, forming a steep front. For diffusion-dominated case, however, capillary effects dominate, producing a significantly broader and more gradual front.

Moreover, the simulations are performed using the BP sweeping technique, whose performance is illustrated in Table 5. For the convection-dominated problem, the bounds to be preserved are determined by the initial condition and set to $[\theta_I, \theta_0]$, whereas for diffusion-dominated problems, the non-homogeneous Neumann condition leads to a physical upper bound, and the preserved range is set to $[\theta_I, \theta_s]$. As can be seen, the BP sweeping technique is essential—it not only enforces physically meaningful bounds on the numerical solutions but also determines whether the simulation can proceed stably.

Example 4.4. *1D water infiltration problem*

This example, based on the Van Genuchten-Mualem model (2.4), originates from the work of Celia et al. [11] and has subsequently been adopted in studies [23, 28, 51]. It considers a 0.6 m soil column representative of New Mexico soils, with parameters given by

$$\theta_r = 0.102,\ \theta_s = 0.368,\ \alpha = 3.35\,\mathrm{m}^{-1},\ K_s = 9.22 \times 10^{-5}\,\mathrm{m/s},\ n = 2,\ m = \frac{1}{2}.$$

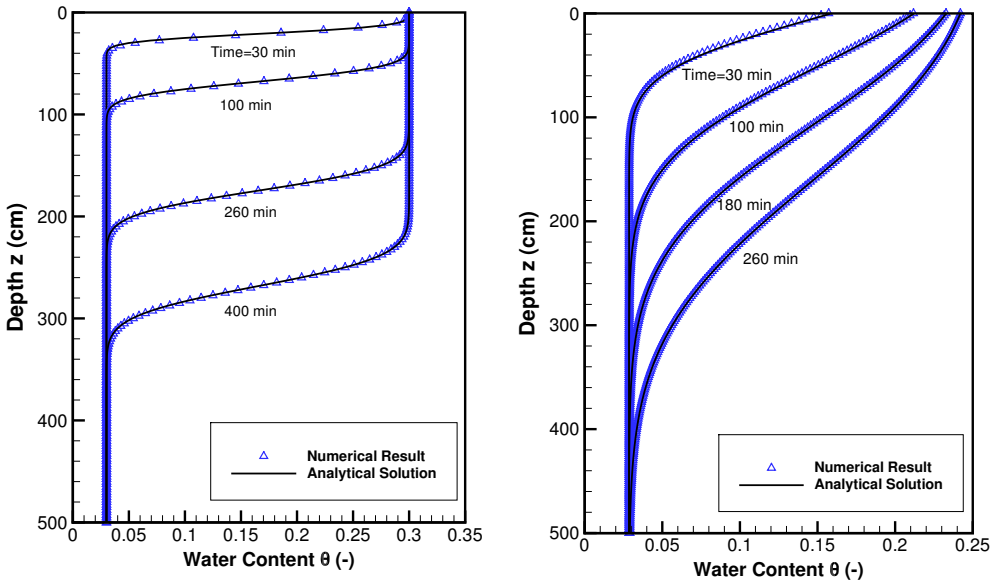

(a) Convection-dominated problem (b) Diffusion-dominated problem

Figure 1. Example 4.3: Numerical solutions of EIN-MRWENO scheme on the grid with $h = 2$.

The boundary conditions for the pressure head are set as $\psi(0,t) = -0.75\,\mathrm{m}$ and $\psi(0.6,t) = -10\,\mathrm{m}$, corresponding to moisture content values of $\theta(0,t) = 0.20037$ and $\theta(0.6,t) = 0.10994$. The initial pressure head distribution is set to

$$\psi(z,0) = \begin{cases} -10, & z \geq 0.006, \\ -0.75 - \frac{9.25}{0.006} z, & 0 \leq z < 0.006. \end{cases}$$

Numerical simulations are performed to obtain the pressure head and moisture content at various times with $C_u = 0.1$, as presented in Figure 2. The reference solutions are taken from Kavetski et al. [28], and good agreement with our results is observed. After 95000 s, the wetting front has propagated through the entire 0.6 m soil column. This benchmark represents the hydrologic response of typical arid and semi-arid soils under a wetting top boundary, which is relevant for assessing water movement and redistribution in rainfall infiltration and irrigation management.

Example 4.5. *1D free drainage problem*

This example is a free drainage problem in a 6 m deep lysimeter performed at the Los Alamos

Table 5. Numerical errors and orders of Example 4.3

		Convection-dominated problem		Diffusion-dominated problem	
	Time	$\theta_{\min} - \theta_m$	$\theta_M - \theta_{\max}$	$\theta_{\min} - \theta_m$	$\theta_M - \theta_{\max}$
Without BP sweeping	30	-4.16E-05	7.99E-05	NaN	NaN
	100	-7.59E-08	-1.91E-08	NaN	NaN
	260	-1.18E-09	-3.07E-11	NaN	NaN
	400	-2.39E-11	-9.46E-14	NaN	NaN
With BP sweeping	30	0	6.70E-05	0	0.16
	100	0	0	0	0.12
	260	0	0	1.99E-07	0.11
	400	0	0	7.14E-04	0.11

Note: The entry "NaN" (Not a Number) indicates an invalid complex result caused by numerical solutions exceeding the physical bound.

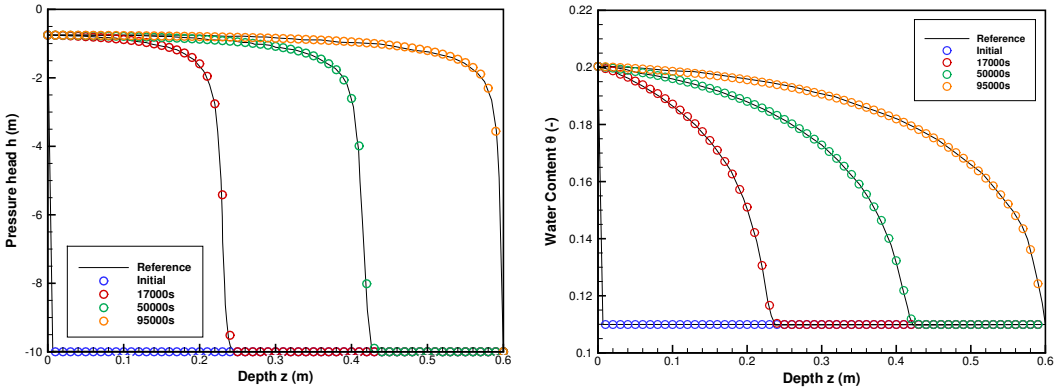

(a) Pressure head h (b) Water content θ

Figure 2. Example 4.4: Numerical solutions of EIN-MRWENO scheme on the grid with $h = 0.01$.

National Laboratory. The van Genuchten-Mualem model (2.4) parameters are given by

$$\theta_r = 0.0,\ \theta_s = 0.33,\ \alpha = 1.43\,\mathrm{m}^{-1},\ K_s = 0.2496\,\mathrm{m/day},\ n = 1.506.$$

The soil column is initially fully saturated, and drainage is driven by gravity under a zero-flux boundary condition at the top and a fixed pressure head $\psi = 0$ at the bottom. In the computations of (3.5) and (3.6), a small perturbation $\epsilon_I = 10^{-5}$ is introduced to redefine the initial and bottom boundary values as $\theta_s - \epsilon_I$, thereby avoiding numerical singularities in γ_D and γ_C caused by $C(\psi) = 0$ at saturation.

Figure 3 presents the pressure head and water content distributions at $t = 1$, 4, 20, 100 days. Good agreement is observed between the numerical results and the experimental data reported in [17, 62, 63], which successfully reproduces the long-term transition from saturated to unsaturated states under gravity. The results provide useful information for predicting drainage rates and equilibrium water retention in initially saturated soils.

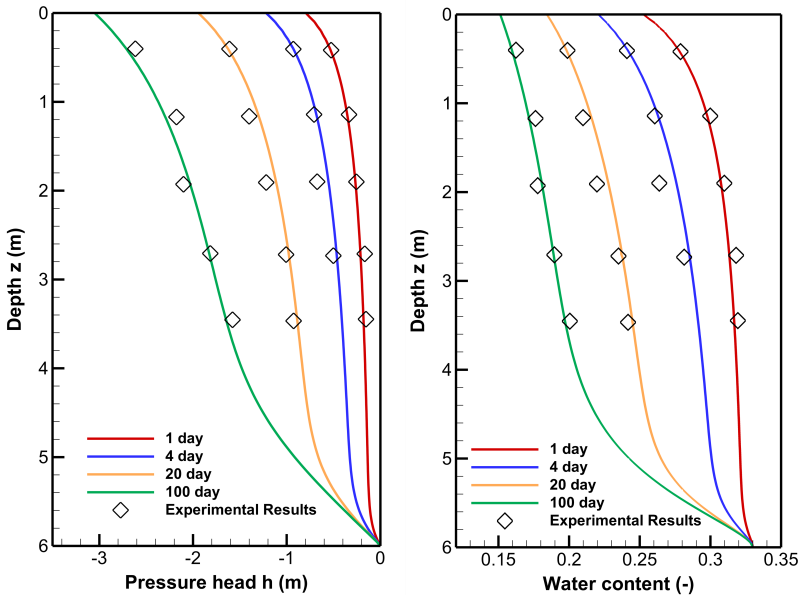

(a) Pressure head ψ (b) Water content θ

Figure 3. Example 4.5: Numerical solutions of EIN-MRWENO scheme on the grid with $h = 0.05$.

Example 4.6. *2D/3D center infiltration problems*

In this example, we consider a 2D/3D infiltration problem with an analytical solution derived by Tracy [55, 56] based on the exponential model (2.6). The parameters are adopted from [69], given as

$$\theta_s = 0.35,\ \theta_r = 0.14,\ K_s = 1 \times 10^{-4}\,\mathrm{m/h},\ \rho = 2 \times 10^{-5}\,\mathrm{m}^{-1},\ \beta = 1.$$

We consider a homogeneous soil domain in the form of a rectangular parallelepiped with boundaries $0 \le x \le a$, $0 \le y \le b$, and $0 \le z \le L$. For the 2D case, we set $a = L = 1\,\mathrm{m}$, while the 3D computational domain is $10 \times 6 \times 8\,\mathrm{m}$. The initial pressure head is fixed at $\psi_r = -1\,\mathrm{m}$. At the top surface of the soil, a Dirichlet boundary condition is imposed for the pressure head, which

takes the value zero at the center and decays smoothly toward the domain edges, i.e.

$$\psi(x, y, z = 1, t) = \frac{1}{\rho} \ln \left(\exp(\rho\psi_r) + (1 - \exp(\rho\psi_r)) \sin(\frac{\pi x}{a}) \sin(\frac{\pi y}{b}) \right).$$

All other boundaries are subject to the constant pressure head condition $\psi_r = -1$. The corresponding analytical solution reads

$$\psi(x, y, z, t) = \frac{1}{\rho} \ln \left(\exp(\rho\psi_r) + \bar{\psi} \right),$$

where

$$\begin{aligned} \bar{\psi} =& \frac{2(1 - \exp(\rho\psi_r))}{Lc} \sin(\frac{\pi x}{a}) \sin(\frac{\pi y}{b}) \exp(\rho(L - z)/2) \sum_{k=1}^{\infty} \left((-1)^k \frac{\lambda_k}{\gamma} \sin(\lambda_k z) \exp(-\gamma t) \right) \\ &+ (1 - \exp(\rho\psi_r)) \sin(\frac{\pi x}{a}) \sin(\frac{\pi y}{b}) \exp(\rho(L - z)/2) \frac{\sinh(\beta z)}{\sinh(\beta L)}, \end{aligned}$$

$$\beta = \sqrt{\rho^2/4 + (\pi/a)^2 + (\pi/b)^2},\ \lambda_k = k\pi/L,\ \gamma = (\beta^2 + \lambda_k^2)/c,\ c = \rho(\theta_s - \theta_r)/Ks.$$

Due to the top boundary condition exhibiting rapidly decaying high-frequency components, we adopt a small $C_u = 2 \times 10^{-5}$ to ensure computational accuracy for short termination times.

The 2D and 3D distributions of the pressure head are displayed in Figures 4 and 5, respectively. To better illustrate the 3D internal structures, we also plot the cross-sectional slices at $x = 2,\ 5,\ 8\,\mathrm{m}$ in Figure 6. It can be clearly observed that the numerical solutions agree excellently with the analytical counterparts. A localized high-permeability zone forms at the center of the top surface, from which water infiltrates downward and laterally, creating a bowl-shaped wetting front that gradually approaches a steady state under long-term simulation. Moreover, the diffusion coefficient in this example is very high ($D \approx 23.81\,\mathrm{m}^2/\mathrm{h}$), which amplifies the efficiency advantage of the EIN method, as demonstrated in Table 7. This case can provide a guidance for understanding water infiltration processes under drip irrigation or localized leakage sources.

Example 4.7. *3D homogeneous infiltration problem*

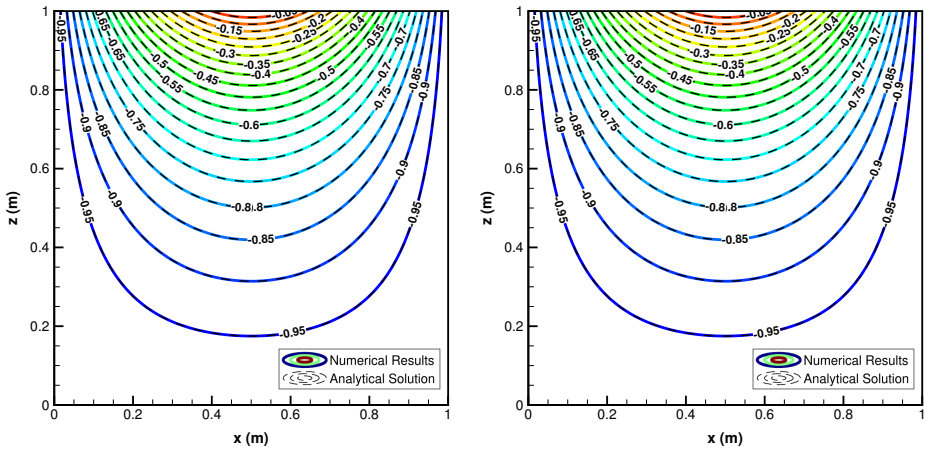

(a) $t = 0.2$ hour (b) $t = 1$ hour

Figure 4. Example 4.6: 2D pressure head of EIN-MRWENO scheme at various times on the grid with $h = 0.01$.

A 3D infiltration process in the homogeneous sand matrix is simulated using the Van Genuchten-Mualem model (2.4), following the setup in [39]. The computational domain is $[0, 2] \times [0, 2] \times [0, 2.6]\,\mathrm{m}$, and the soil is initially dry with $\psi = -0.3\,\mathrm{m}$ ($\theta = 0.185$). A constant pressure head $\psi = -0.1\,\mathrm{m}$ ($\theta = 0.2955$) is prescribed on the top boundary, while a flux condition $\nabla\psi \cdot \mathbf{n} = 1$ is imposed at the bottom, with $\mathbf{n}$ denoting the outward unit normal. All other boundaries are subjected to no-flow conditions. The soil hydraulic parameters are given by

$$\theta_r = 0.02,\ \theta_s = 0.417,\ \alpha = 13.8\,\mathrm{m}^{-1},\ K_s = 5.03712\,\mathrm{m/day},\ n = 1.592.$$

Figure 7 presents the simulated pressure head distribution, which shows good agreement with the reference solution reported in [39]. Due to the homogeneous sand matrix and uniform top boundary condition, a downward-propagating wetting front forms and remains horizontal throughout the simulation. Meanwhile, the impermeable bottom boundary leads to a gradual increase in pressure head at the bottom.

Example 4.8. *3D infiltration problem in layered soil*

We further simulate an infiltration problem in an L-shaped layered soil. The computational domain is a $1\,\mathrm{m}^3$ cube with two distinct materials arranged in an L-shaped configuration, as shown in

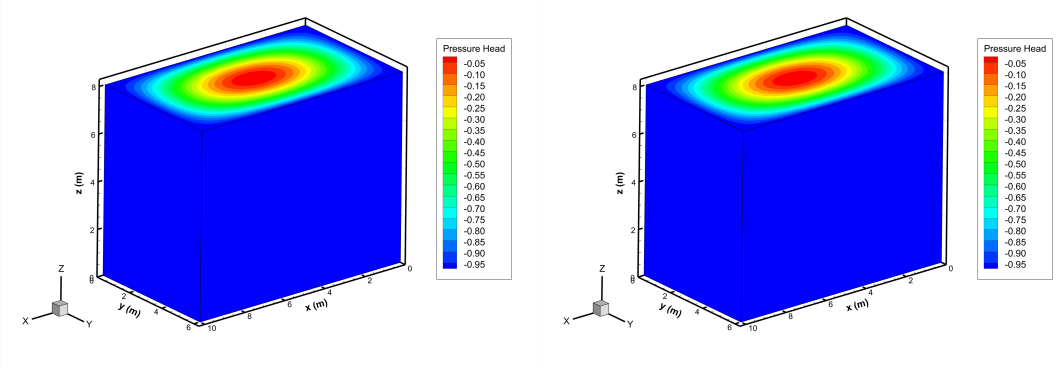

(a) $t = 0.1$ hour (b) $t = 1$ hour

Figure 5. Example 4.6: 3D pressure head of EIN-MRWENO scheme at various times on the grid with $h = 0.2$.

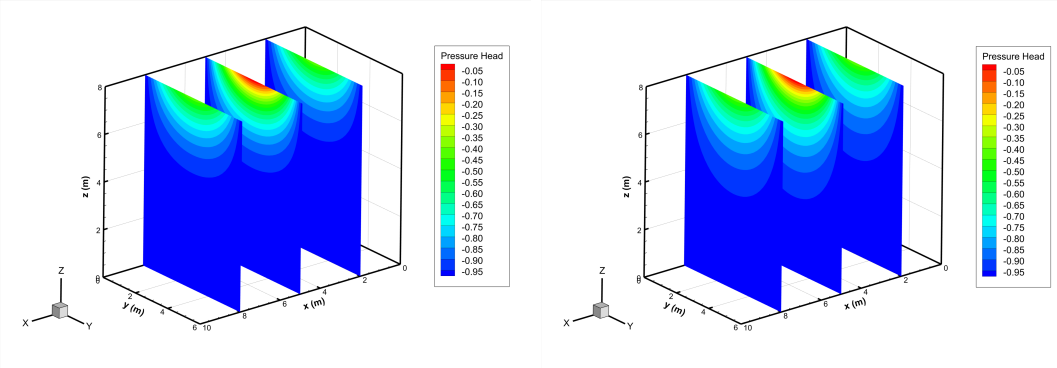

(a) $t = 0.1$ hour (b) $t = 1$ hour

Figure 6. Example 4.6: The slice planes of 3D pressure head of EIN-MRWENO scheme at various times on the grid with $h = 0.2$.

Figure 8. Clay occupies the top layer ($z \leq 0.2$) and the left column extending to $z \leq 0.8$ for $x \leq 0.5$, while the remainder of the domain is filled with silt. The Van Genuchten-Mualem model (2.4) is adopted, with its parameters for the two soil types taken from [64] and listed in Table 6. The initial condition is set as $\psi = -10\,\mathrm{m}$. A fixed-head boundary condition of $\psi = -0.2\,\mathrm{m}$ is applied at the top side, while a free drainage boundary condition $q = K(\psi)$ is imposed at the bottom side. The remaining boundaries are considered impermeable.

We simulate the evolution of pressure head and water content at different times with $C_u = 0.1$, see Figures 9 and 10. As illustrated, an interesting non-uniform infiltration pattern induced by the L-shaped layered distribution is captured by our method. The clay region exhibits faster

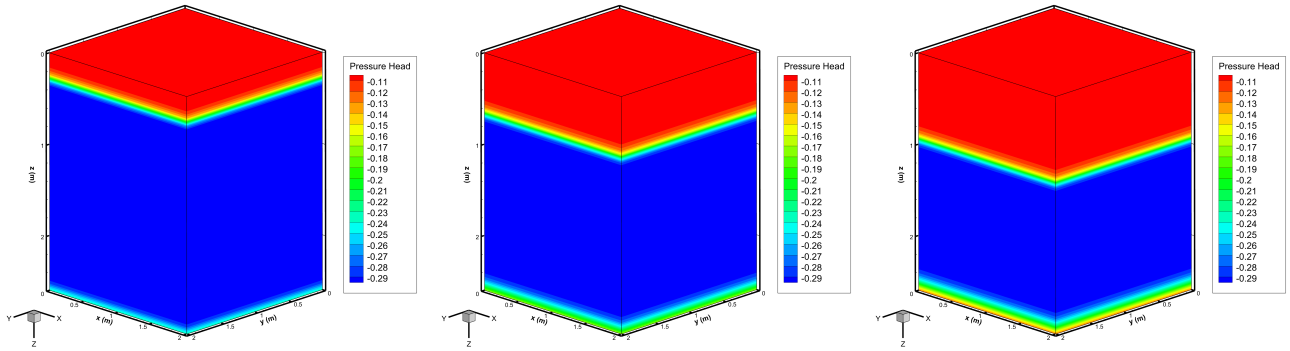

(a) $t = 0.2$day (b) $t = 0.6$day (c) $t = 0.9$day

Figure 7. Example 4.7: Pressure head of EIN-MRWENO scheme at various times on the grid with $h = 0.02$.

infiltration with a deeper wetting front, while the silt region shows slower infiltration. Additionally, at the clay-silt interface, lateral water diffusion from clay to silt is observed, resulting in localized water accumulation.

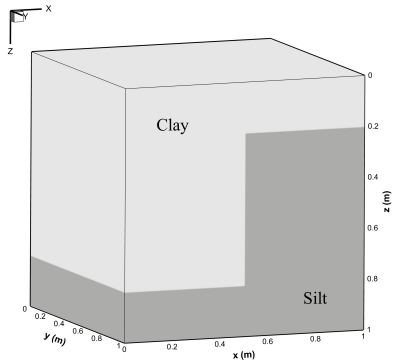

Figure 8. Example 4.8: L-shaped layered soil geometry.

Example 4.9. *3D heterogeneous infiltration problem*

In this example, we use our scheme to solve a 3D infiltration problem in heterogeneous soil media. The $1\,\mathrm{m}^3$ cubic computational domain is filled with four types of loam soil following a uniform random distribution, see Figure 11. The hydraulic properties are governed by the Van Genuchten-Mualem model (2.4), with parameters for the four soil types provided in Table 6. Initially, the entire domain is at a pressure head of $\psi = -2\,\mathrm{m}$. Infiltration is driven by a constant head

Table 6. The soil hydraulic parameters

Soil type	θ_r	θ_s	α (m^{-1})	K_s (m/day)	n
Clay	0.068	0.38	0.80	0.048	1.09
Silt	0.034	0.46	1.60	0.06	1.37
Loam	0.078	0.43	3.60	0.2496	1.56
Silt loam	0.067	0.45	2.00	0.1038	1.41
Clay loam	0.095	0.41	1.90	0.0624	1.31
Silty clay loam	0.089	0.43	1.00	0.0168	1.23

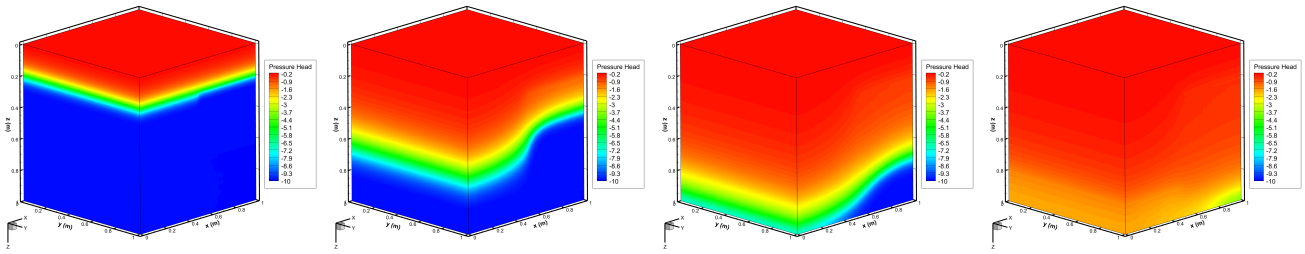

(a) $t = 1$ day (b) $t = 10$ day (c) $t = 30$ day (d) $t = 50$ day

Figure 9. Example 4.8: Pressure head of EIN-MRWENO scheme at various times on the grid with $h = 0.02$.

$\psi = -0.5\,\mathrm{m}$ prescribed at the top surface, while free drainage ($q = K(\psi)$) is allowed at the bottom. All other lateral boundaries are set to be impermeable.

The resulting evolution of water content with $C_u = 0.1$ is depicted in Figure 12, demonstrating the effectiveness of the proposed method in handling heterogeneous soil configurations. In contrast to the results for homogeneous cases, e.g. Figure 7, the wetting front exhibits a highly heterogeneous structure characterized by spatially varying penetration depths. High-permeability zones act

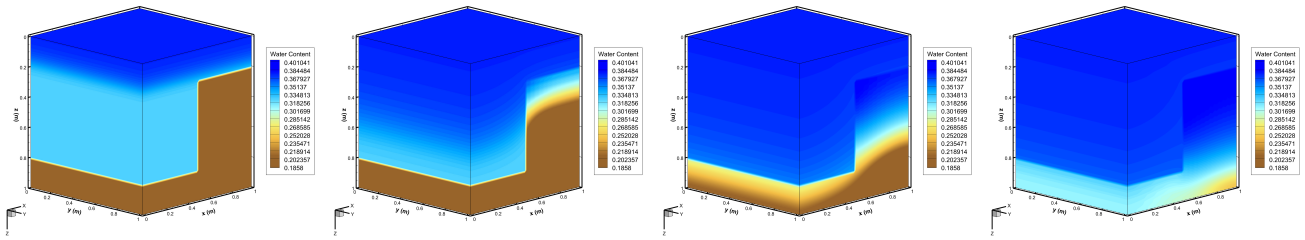

(a) $t = 1$ day (b) $t = 10$ day (c) $t = 30$ day (d) $t = 50$ day

Figure 10. Example 4.8: Water content of EIN-MRWENO scheme at various times on the grid with $h = 0.02$.

as dominant flow pathways, allowing water to penetrate deeper and faster, while low-permeability zones impede the advance of water, resulting in shallower wetting fronts. This highlights the importance of incorporating soil heterogeneity in accurate hydrological and geotechnical simulations.

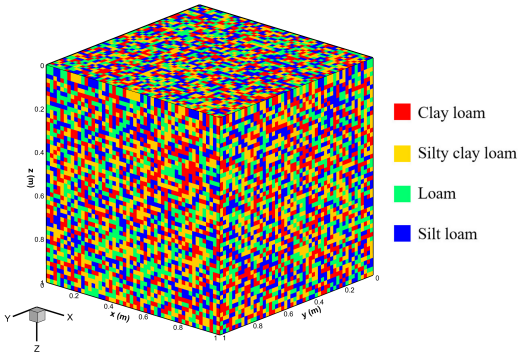

Figure 11. Example 4.9: Heterogeneous soil classes.

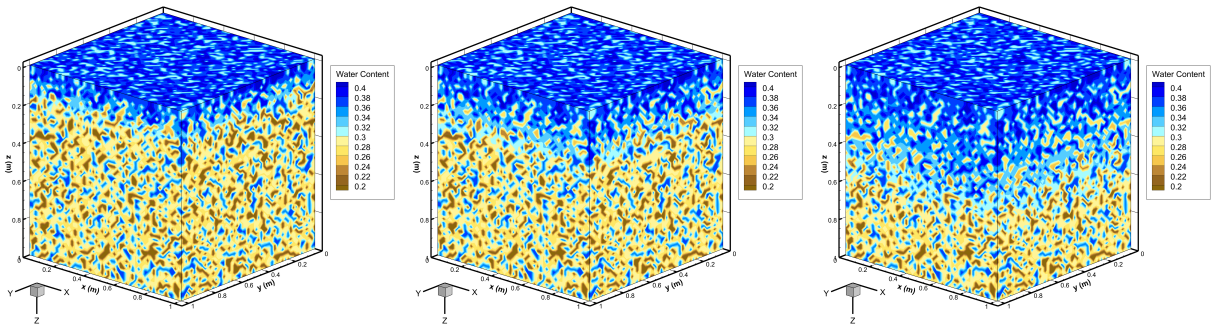

(a) $t = 1$ day (b) $t = 3$ day (c) $t = 9$ day

Figure 12. Example 4.9: Water content of EIN-MRWENO scheme at various times on the grid with $h = 0.02$.

Example 4.10. *3D realistic infiltration problem*

To provide a realistic assessment of transient water infiltration as an indicator for contaminant transport in loam soils, we simulate infiltration in the black soil region of Northeast China. As a major agricultural production base, this region is critical to national food security and ecological stability. Accurate simulation of water infiltration is therefore essential for formulating sustainable agricultural water management strategies.

This example is inspired by [22, 51], where reference solutions can be found for comparison. A random surface topography $z_0(x, y)$ is generated to capture natural soil variability, yielding a 3D

computational domain $[0,12]\times[0,6]\times[z_0,3]\,\mathrm{m}$. The irregular top surface z_0 at point (x,y) is a random variable fluctuating around zero. The initial pressure head is uniformly set to $\psi=-20\,\mathrm{m}$, with a constant pressure head $\psi=-2\,\mathrm{m}$ prescribed on the irregular top surface. No-flow conditions ($q=0$) are imposed on the four lateral boundaries and the bottom. The hydraulic properties obey the Van Genuchten-Mualem relation (2.4). Soil samples collected from the black soil region were subjected to particle size analysis, yielding a texture composition of 19.8% sand, 42.5% silt, and 37.7% clay. The parameters were estimated using HYDRUS based on the textural data and are listed as follows:

$$\theta_r=0.0904,\ \theta_s=0.4672,\ \alpha=1.10\,\mathrm{m}^{-1},\ K_s=0.1239\,\mathrm{m/day},\ n=1.4159,\ m=1-\frac{1}{n}.$$

To accommodate the irregular top boundary, the physical domain is mapped onto a regular computational space via the coordinate transformation

$$\xi=x,\ \eta=y,\ \zeta=\frac{3(z-z_0(x,y))}{3-z_0(x,y)}.$$

Let $J=\det\left(\frac{\partial(x,y,z)}{\partial(\xi,\eta,\zeta)}\right)$ denote the Jacobian determinant. Under this transformation, the governing equation becomes

$$\begin{aligned}\frac{\partial(J\theta)}{\partial t}=&\frac{\partial}{\partial\xi}\left(JK(\psi)\left(\frac{\partial\psi}{\partial\xi}+A\frac{\partial\psi}{\partial\zeta}\right)\right)+\frac{\partial}{\partial\eta}\left(JK(\psi)\left(\frac{\partial\psi}{\partial\eta}+B\frac{\partial\psi}{\partial\zeta}\right)\right)\\&+\frac{\partial}{\partial\zeta}\left(JK(\psi)\left(A\frac{\partial\psi}{\partial\xi}+B\frac{\partial\psi}{\partial\eta}+(A^2+B^2+C^2)\frac{\partial\psi}{\partial\zeta}\right)\right)-\frac{\partial(JK(\psi)C)}{\partial\zeta},\end{aligned}$$

where

$$A=\frac{\partial\zeta}{\partial x}=\frac{\partial z_0}{\partial\xi}\cdot\frac{\zeta-3}{3-z_0(\xi,\eta)},\ B=\frac{\partial\zeta}{\partial y}=\frac{\partial z_0}{\partial\eta}\cdot\frac{\zeta-3}{3-z_0(\xi,\eta)},\ C=\frac{\partial\zeta}{\partial z}=\frac{3}{3-z_0(\xi,\eta)},\ J=\frac{1}{C}.$$

The resulting water content distributions at different times with $C_u=0.2$ are presented in Figure 13, illustrating the gradual downward progression of the wetting front with spatially varying

infiltration depths. In regions with lower surface elevation, the shorter infiltration distance allows the wetting front to reach the impermeable bottom more quickly. Subsequently, water accumulates to form a nearly saturated zone and then expands upward and laterally, which is a critical process for assessing groundwater recharge and soil waterlogging risk.

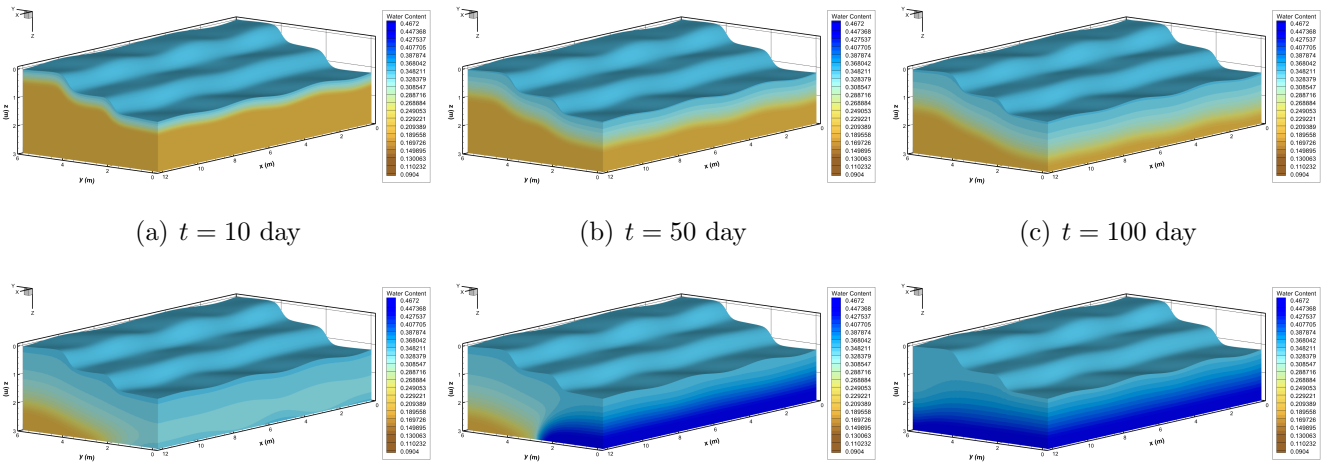

(a) $t = 10$ day (b) $t = 50$ day (c) $t = 100$ day

(d) $t = 200$ day (e) $t = 240$ day (f) $t = 320$ day

Figure 13. Example 4.10: Water content θ of EIN-MRWENO scheme at various times on the grid with $h = 0.1$.

4.3. Computational efficiency

In order to further illustrate the high efficiency of the EIN-MRWENO scheme, we compare the computational cost with that of the SSPRK-MRWENO scheme for the application cases presented in Section 4.2. Table 7 reports the CPU times and efficiency ratios for the various cases considered. Combined with the results presented in Tables 1-3, it can be observed that the CPU time required by the EIN-MRWENO scheme is significantly less than that of the SSPRK-MRWENO scheme, particularly for cases involving high diffusion coefficients, small mesh sizes, high-dimensional problems, and complex simulations.

5. Conclusions

This paper presents a comprehensive numerical investigation of the Richards equation, overcoming the long-standing challenges in unsaturated flow simulations, including undesired accuracy,

Table 7. Comparison of CPU time between the EIN-MRWENO and SSPRK-MRWENO schemes for different test cases

Cases	EIN-MRWENO(s)	SSPRK-MRWENO(s)	Radio	Savings
Ex 4.3-Convection	0.5973	0.3611	0.60	-
Ex 4.3-Diffusion	0.6749	2.3522	3.49	71.31%
Ex 4.4	1.3071	2.1136	1.62	38.16%
Ex 4.5	17345.6381	23450.7018	1.35	26.03%
Ex 4.6-2D	488.7553	2413098.8312	4937.23	99.98%
Ex 4.6-3D	465.4612	10754.498837	23.11	95.67%
Ex 4.7	1511.889799	3529.533592	2.33	57.16%
Ex 4.8	4103.7270	15925.2104	3.88	74.23%
Ex 4.9	3620.9129	37330.7345	10.31	90.30%
Ex 4.10	25546.59456	253016.2753	9.90	89.90%

low computational efficiency, and insufficient robustness. We have developed an efficient high-order EIN time-marching scheme with a conservative MRWENO spatial discretization for the Richards equation in mass-conservative form. A bound-preserving sweeping technique has been incorporated to maintain physical admissibility of the numerical solutions. The main findings of this paper can be summarized as follows:

- The proposed EIN-MRWENO scheme achieves third-order accuracy in both space and time, enabling precise resolution of sharp wetting fronts.

- The EIN scheme relaxes the time-step restriction while eliminating costly nonlinear iterations. Computational efficiency analyses demonstrate significant speedup compared to the explicit SSP-RK method, with savings proportional to the grid size—reaching up to 90%, sometimes even up to 99%, for highly refined meshes, large diffusion coefficients and complex simulations, making large-scale and high-resolution geotechnical simulations practically feasible.

- The BP sweeping technique does not compromise the high-order accuracy of the underlying scheme, and is essential for almost all application cases to prevent simulation instability or even computational failure.

- Systematic comparisons with benchmark reference solutions and experimental data confirm

the excellent performance and reliability of the proposed method.

- By conducting infiltration and drainage simulations across three distinct hydraulic models, one- to three-dimensional spaces, layered and heterogeneous soils, and irregular geometries, the proposed method is demonstrated considerable universality and capability of handling complex problems, thereby providing a powerful computational engine and valuable insights for practical geotechnical engineering applications.

Future work will consider extending the framework to coupled multiphysics problems, such as reactive transport in porous media, where the Richards equation serves as the flow component.

References

[1] Abriola, L.M., Lang, J.R., 1990. Self-adaptive hierarchic finite element solution of the one-dimensional unsaturated flow equation. *International Journal for Numerical Methods in Fluids*, 10(3), 227–246.

[2] Arbogast, T., Wheeler, M.F., 1996. A nonlinear mixed finite element method for a degenerate parabolic equation arising in flow in porous media. *SIAM Journal on Numerical Analysis*, 33(4), 1669–1687.

[3] Ascher, U.M., Ruuth, S.J., Spiteri, R.J., 1997. Implicit-explicit Runge-Kutta methods for time-dependent partial differential equations. *Applied Numerical Mathematics*, 25(2-3), 151–167.

[4] Balsara, D.S., Shu, C.-W., 2000. Monotonicity preserving weighted essentially non-oscillatory schemes with increasingly high order of accuracy. *Journal of Computational Physics*, 160(2), 405–452.

[5] Basha, H., 1999. Multidimensional linearized nonsteady infiltration with prescribed boundary conditions at the soil surface. *Water Resources Research*, 35(1), 75–83.

[6] Bause, M., Knabner, P., 2004. Computation of variably saturated subsurface flow by adaptive mixed hybrid finite element methods. *Advances in Water Resources*, 27(6), 565–581.

[7] Boujoudar, M., Beljadid, A., Taik, A., 2021. Localized MQ-RBF meshless techniques for modeling unsaturated flow. *Engineering Analysis with Boundary Elements*, 130, 109–123.

[8] Boujoudar, M., Beljadid, A., Taik, A., 2023. Localized RBF methods for modeling infiltration using the kirchhoff-transformed Richards equation. *Engineering Analysis with Boundary Elements*, 152, 259–276.

[9] Brooks, R.H., Corey, A.T., et al., 1964. Hydraulic properties of porous media and their relation to drainage design. *Transactions of the ASAE*, 7(1), 26–28.

[10] Celia, M.A., Ahuja, L.R., Pinder, G.F., 1987. Orthogonal collocation and alternating-direction procedures for unsaturated flow problems. *Advances in Water Resources*, 10(4), 178–187.

[11] Celia, M.A., Bouloutas, E.T., Zarba, R.L., 1990. A general mass-conservative numerical solution for the unsaturated flow equation. *Water Resources Research*, 26(7), 1483–1496.

[12] Chávez-Negrete, C., Domínguez-Mota, F., Santana-Quinteros, D., 2018. Numerical solution of Richards' equation of water flow by generalized finite differences. *Computers and Geotechnics*, 101, 168–175.

[13] Cote, C.M., Bristow, K.L., Charlesworth, P.B., Cook, F.J., Thorburn, P.J., 2003. Analysis of soil wetting and solute transport in subsurface trickle irrigation. *Irrigation Science*, 22(3), 143–156.

[14] Dogan, A., Motz, L.H., 2005. Saturated-unsaturated 3D groundwater model. I: Development. *Journal of Hydrologic Engineering*, 10(6), 492–504.

[15] Douglas Jr, J., Dupont, T., 1971. Alternating-direction Galerkin methods on rectangles, in: Numerical Solution of Partial Differential Equations–II. Elsevier, pp. 133–214.

[16] Duchemin, L., Eggers, J., 2014. The explicit-implicit-null method: Removing the numerical instability of PDEs. *Journal of Computational Physics*, 263, 37–52.

[17] Forsyth, P.A., Wu, Y., Pruess, K., 1995. Robust numerical methods for saturated-unsaturated flow with dry initial conditions in heterogeneous media. *Advances in Water Resources*, 18(1), 25–38.

[18] Gardner, W.R., 1958. Some steady state solutions of unsaturated moisture flow equations with applications to evaporation from a water table. *Soil Science*, 85(4), 228–232.

[19] Hajduk, H., 2021. Monolithic convex limiting in discontinuous Galerkin discretizations of hyperbolic conservation laws. *Computers & Mathematics with Applications*, 87, 120–138.

[20] Haverkamp, R., Vauclin, M., Touma, J., Wierenga, P., Vachaud, G., 1977. A comparison of numerical simulation models for one-dimensional infiltration. *Soil Science Society of America Journal*, 41(2), 285–294.

[21] Hills, R., Porro, I., Hudson, D., Wierenga, P., 1989. Modeling one-dimensional infiltration into very dry soils: 1. model development and evaluation. *Water Resources Research*, 25(6), 1259–1269.

[22] Horgue, P., Franc, J., Guibert, R., Debenest, G., 2015a. An extension of the open-source porousmultiphasefoam toolbox dedicated to groundwater flows solving the Richards' equation. *arXiv preprint arXiv:1510.01364*, .

[23] Horgue, P., Soulaine, C., Franc, J., Guibert, R., Debenest, G., 2015b. An open-source toolbox for multiphase flow in porous media. *Computer Physics Communications*, 187, 217–226.

[24] Huang, K., Zhang, R., Van Genuchten, M.T., 1994. An Eulerian-Lagrangian approach with an adaptively corrected method of characteristics to simulate variably saturated water flow. *Water Resources Research*, 30(2), 499–507.

[25] Jaiswal, D.K., Kumar, A., Yadav, R.R., 2011. Analytical solution to the one-dimensional advection-diffusion equation with temporally dependent coefficients. *Journal of Water Resource and Protection*, 3(1), 76.

[26] Jiang, Y., Xu, Z., 2013. Parametrized maximum principle preserving limiter for finite difference WENO schemes solving convection-dominated diffusion equations. *SIAM Journal on Scientific Computing*, 35(6), A2524–A2553.

[27] Jiang, G.-S., Shu, C.-W., 1996. Efficient implementation of weighted ENO schemes. *Journal of Computational Physics*, 126(1), 202–228.

[28] Kavetski, D., Binning, P., Sloan, S., 2001. Adaptive time stepping and error control in a mass conservative numerical solution of the mixed form of Richards equation. *Advances in Water Resources*, 24(6), 595–605.

[29] Kavetski, D., Binning, P., Sloan, S.W., 2002a. Adaptive backward Euler time stepping with truncation error control for numerical modelling of unsaturated fluid flow. *International Journal for Numerical Methods in Engineering*, 53(6), 1301–1322.

[30] Kavetski, D., Binning, P., Sloan, S.W., 2002b. Noniterative time stepping schemes with adaptive truncation error control for the solution of Richards equation. *Water Resources Research*, 38(10), 29–1.

[31] Keita, S., Beljadid, A., Bourgault, Y., 2021. Implicit and semi-implicit second-order time stepping methods for the Richards equation. *Advances in Water Resources*, 148, 103841.

[32] Koto, T., 2008. IMEX Runge-Kutta schemes for reaction-diffusion equations. *Journal of Computational and Applied Mathematics*, 215(1), 182–195.

[33] Kuzmin, D., 2020. Monolithic convex limiting for continuous finite element discretizations of hyperbolic conservation laws. *Computer Methods in Applied Mechanics and Engineering*, 361, 112804.

[34] Lai, W., Ogden, F.L., 2015. A mass-conservative finite volume predictor-corrector solution of the 1D Richards' equation. *Journal of Hydrology*, 523, 119–127.

[35] Lehmann, F., Ackerer, P., 1998. Comparison of iterative methods for improved solutions of the fluid flow equation in partially saturated porous media. *Transport in Porous Media*, 31(3), 275–292.

[36] Li, H., Farthing, M., Dawson, C., Miller, C., 2007. Local discontinuous Galerkin approximations to Richards' equation. *Advances in Water Resources*, 30(3), 555–575.

[37] Liu, X.D., Osher, S., Chan, T., 1994. Weighted essentially non-oscillatory schemes. *Journal of Computational Physics*, 115(1), 200–212.

[38] Liu, Y., Cheng, Y., Shu, C.-W., 2017. A simple bound-preserving sweeping technique for conservative numerical approximations. *Journal of Scientific Computing*, 73(2), 1028–1071.

[39] Liu, Y., Yang, H., Xie, Z., Qin, P., Li, R., 2020. Parallel simulation of variably saturated soil water flows by fully implicit domain decomposition methods. *Journal of Hydrology*, 582, 124481.

[40] Manzini, G., Ferraris, S., 2004. Mass-conservative finite volume methods on 2-D unstructured grids for the Richards' equation. *Advances in Water Resources*, 27(12), 1199–1215.

[41] Namin, M.M., Boroomand, M.R., 2012. A time splitting algorithm for numerical solution of Richard's equation. *Journal of Hydrology*, 444, 10–21.

[42] Neuman, S.P., 1973. Saturated-unsaturated seepage by finite elements. *Journal of the Hydraulics Division*, 99(12), 2233–2250.

[43] Ogden, F.L., Lai, W., Steinke, R.C., Zhu, J., Talbot, C.A., Wilson, J.L., 2015. A new general 1-D vadose zone flow solution method. *Water Resources Research*, 51(6), 4282–4300.

[44] Oulhaj, A.A.H., Cancès, C., Chainais-Hillairet, C., 2018. Numerical analysis of a nonlinearly stable and positive control volume finite element scheme for Richards equation with anisotropy. *ESAIM: Mathematical Modelling and Numerical Analysis*, 52(4), 1533–1567.

[45] Paniconi, C., Aldama, A.A., Wood, E.F., 1991. Numerical evaluation of iterative and noniterative methods for the solution of the nonlinear Richards equation. *Water Resources Research*, 27(6), 1147–1163.

[46] Richards, L.A., 1931. Capillary conduction of liquids through porous mediums. *Physics*, 1(5), 318–333.

[47] Romano, N., Brunone, B., Santini, A., 1998. Numerical analysis of one-dimensional unsaturated flow in layered soils. *Advances in Water Resources*, 21(4), 315–324.

[48] Shahraiyni, H.T., Ataie-Ashtiani, B., 2012. Mathematical forms and numerical schemes for the solution of unsaturated flow equations. *Journal of Irrigation and Drainage Engineering*, 138(1), 63–72.

[49] Shu, C.-W., 2009. High order weighted essentially nonoscillatory schemes for convection dominated problems. *SIAM Review*, 51(1), 82–126.

[50] Šimůnek, J., Van Genuchten, M.T., Šejna, M., et al., 2006. The HYDRUS software package for simulating two-and three-dimensional movement of water, heat, and multiple solutes in variably-saturated media. *Technical Manual, Version*, 1, 241.

[51] Su, X., Zhang, M., Zou, D., Zhao, Y., Zhang, J., Su, H., 2022. Numerical scheme for solving the Richard's equation based on finite volume model with unstructured mesh and implicit dual-time stepping. *Computers and Geotechnics*, 147, 104768.

[52] Svyatskiy, D., Lipnikov, K., 2017. Second-order accurate finite volume schemes with the discrete maximum principle for solving Richards' equation on unstructured meshes. *Advances in Water Resources*, 104, 114–126.

[53] Tan, M., Cheng, J., Shu, C.-W., 2022. Stability of high order finite difference and local discontinuous Galerkin schemes with explicit-implicit-null time-marching for high order dissipative and dispersive equations. *Journal of Computational Physics*, 464, 111314.

[54] Tan, M., Cheng, J., Shu, C.-W., 2023. Stability of spectral collocation schemes with explicit-implicit-null time-marching for convection-diffusion and convection-dispersion equations. *East Asian Journal on Applied Mathematics*, 13(3), 464–498.

[55] Tracy, F., 2007. Three-dimensional analytical solutions of Richards' equation for a box-shaped soil sample with piecewise-constant head boundary conditions on the top. *Journal of Hydrology*, 336(3-4), 391–400.

[56] Tracy, F.T., 2006. Clean two-and three-dimensional analytical solutions of Richards' equation for testing numerical solvers. *Water Resources Research*, 42, W08503.

[57] Van Genuchten, M.T., 1980. A closed-form equation for predicting the hydraulic conductivity of unsaturated soils. *Soil Science Society of America Journal*, 44(5), 892–898.

[58] Wu, X., Cheng, J., Shu, C.-W., 2026. A high-order bound-preserving finite difference multi-resolution WENO method for high-dimensional Richards equation. *Submitted to Advances in Water Resources*, minor revision under review.

[59] Xiong, T., Qiu, J.M., Xu, Z., 2015. High order maximum-principle-preserving discontinuous Galerkin method for convection-diffusion equations. *SIAM Journal on Scientific Computing*, 37(2), A583–A608.

[60] Xu, Z., 2014. Parametrized maximum principle preserving flux limiters for high order schemes solving hyperbolic conservation laws: one-dimensional scalar problem. *Mathematics of Computation*, 83(289), 2213–2238.

[61] Yang, D., Zhang, T., Zhang, K., Greenwood, D.J., Hammond, J.P., White, P.J., 2009. An eas-

ily implemented agro-hydrological procedure with dynamic root simulation for water transfer in the crop–soil system: validation and application. *Journal of Hydrology*, 370(1-4), 177–190.

[62] Zadeh, K.S., 2011. A mass-conservative switching algorithm for modeling fluid flow in variably saturated porous media. *Journal of Computational Physics*, 230(3), 664–679.

[63] Zambra, C., Dumbser, M., Toro, E.F., Moraga, N., 2012. A novel numerical method of high-order accuracy for flow in unsaturated porous media. *International Journal for Numerical Methods in Engineering*, 89(2), 227–240.

[64] Zha, Y., Yang, J., Yin, L., Zhang, Y., Zeng, W., Shi, L., 2017. A modified picard iteration scheme for overcoming numerical difficulties of simulating infiltration into dry soil. *Journal of Hydrology*, 551, 56–69.

[65] Zhang, X., Liu, Y., Shu, C.-W., 2012. Maximum-principle-satisfying high order finite volume weighted essentially nonoscillatory schemes for convection-diffusion equations. *SIAM Journal on Scientific Computing*, 34(2), A627–A658.

[66] Zhang, X., Shu, C.-W., 2010. On maximum-principle-satisfying high order schemes for scalar conservation laws. *Journal of Computational Physics*, 229(9), 3091–3120.

[67] Zhang, Y., Zhang, X., Shu, C.-W., 2013. Maximum-principle-satisfying second order discontinuous Galerkin schemes for convection–diffusion equations on triangular meshes. *Journal of Computational Physics*, 234, 295–316.

[68] Zhu, J., Shu, C.-W., 2018. A new type of multi-resolution WENO schemes with increasingly higher order of accuracy. *Journal of Computational Physics*, 375, 659–683.

[69] Zhu, S., Wu, L., Shen, Z., Huang, R., 2019. An improved iteration method for the numerical solution of groundwater flow in unsaturated soils. *Computers and Geotechnics*, 114, 103113.